PHYSICAL REVIEW B **88**, 045405 (2013)

Theory of remote phonon scattering in top-gated single-layer graphene

Zhun-Yong Ong[*] and Massimo V. Fischetti[†]
Department of Materials Science and Engineering, University of Texas at Dallas, 800 W Campbell Rd RL10, Richardson, Texas 75080, USA

(Received 23 April 2013; published 2 July 2013)

We extend the theory of interfacial plasmon-phonon scattering to top-gated single-layer graphene. As with bottom-gated graphene, interfacial plasmon-phonon (IPP) modes are formed from the coupling between the graphene plasmon and the surface polar phonon modes in the top and bottom oxides. We study the effect of the top oxide thickness on dynamic screening and electron-IPP coupling. The remote phonon-limited electron mobility μ_{RP} and electron scattering rates in a HfO_2-covered, SiO_2-supported single-layer graphene are computed at various electron densities n for different dielectric thickness t_{ox}. We find that μ_{RP} is much more dependent on t_{ox} at low n. They also agree with the experimentally estimated room temperature μ_{RP} from Zou *et al.* [Phys. Rev. Lett. **105**, 126601 (2010)]. The electron density dependent μ_{RP} is predicted to be between 5500 and 24 200 $\mathrm{cm}^2\mathrm{V}^{-1}\mathrm{s}^{-1}$ from $n = 10^{12}$ to 10^{13} cm^{-2} at 300 K.

DOI: 10.1103/PhysRevB.88.045405 PACS number(s): 79.60.Jv, 73.50.Dn, 74.78.Fk, 72.80.Vp

I. INTRODUCTION

One of the more promising nanoelectronic applications for graphene is in high frequency devices.[1,2] Typically, graphene is physically supported by an insulating dielectric substrate such as SiO_2, and a local top gate, consisting of a layer of high-κ dielectric metal oxide such as HfO_2 or Al_2O_3, can be overlayed on the graphene.[3–7] The top gate offers better electrostatic control of the local carrier density than a bottom gate, and is necessary for the integration of graphene into nanoelectronic applications. However, the top gate must necessarily modify the electrostatic environment of the graphene. For instance, long-range Coulombic impurity scattering is weakened in the presence of a high-κ top oxide,[8] resulting in a possible increase of the electron mobility. On the other hand, the top gate also exposes the graphene to new scattering mechanisms that can degrade electron transport. For example, additional defects are formed when the dielectric is deposited on the graphene. Another is remote scattering by the surface polar phonon (SPP) modes in the top oxide.

Although the subject of remote phonon scattering of electrons in single-layer graphene (SLG),[9–13] including the related carbon nanotubes,[10,11] has been amply discussed before, the basic approach used in the aforementioned works does not deal adequately with the hybridization between the *bare* SPP and graphene plasmon modes, a phenomenon that has been observed experimentally.[14–16] Neither can it explain the dynamic screening of remote interaction with the substrate phonons. More importantly, it is difficult to generalize the method to describe remote phonon scattering in a heterostructure such as a top-gated SLG where the thickness of the top dielectric may affect the scattering processes. It was shown experimentally[17] that a higher-κ overlayer (ice in Ref. 17) on the SLG can weaken Coulombic impurity scattering and lead to a small improvement in the conductivity, although Ponomarenko and co-workers were not able find any significant improvement using a high-κ liquid overlayer. The actual deposition of dielectric oxide material (HfO_2 or Al_2O_3) on the graphene has been found to lead to a degradation of the electron mobility.[3,6,7,18]

In an earlier paper,[19] we developed the theory of interfacial plasmon phonons (IPPs) in supported graphene and showed how the phenomenon of dynamic screening emerges from the coupling between the graphene plasmons and the SPP modes in the substrate.[19,20] Using that theory, we studied the remote IPP scattering of electrons in SLG supported by an insulating substrate, and also applied it to heat transfer between graphene and the substrate.[21] It is not apparent that the model presented in Ref. 19 has any advantage over other existing remote phonon scattering models,[22,23] apart from a more satisfactory account of dynamic screening. Some form of a static screening model[22,23] can be used because the plasmon frequency is usually greater than the frequency of the substrate dipole excitation in supported graphene, except at long wavelengths. However, in this paper, the necessity of dynamic screening becomes manifest because the surrounding oxides modify the dispersion of the plasmons. We extend our theory of interfacial plasmon phonons to top-gated SLG, where oxide dielectrics can be found above and under the SLG sheet. This structure is also called a *double-oxide* structure[24] in the literature. The top and bottom oxides contain SPP modes which interact with the SLG. This extension of the IPP theory is nontrivial because we have to take into account the finite thickness of the top oxide and also the coupling of the top and bottom dipole fields.

Let us give a foretaste of the remaining content by describing the problem of dynamic screening in top-gated SLG with an ultrathin top-gate dielectric. When t_{ox} is very small (around 2 nm), the image charge distribution in the metal substantially weakens the effective electron-electron interaction and downshifts the plasmon frequencies, i.e., the plasmons are "softened."Given that the screening of a remote excitation occurs when the corresponding plasmon frequency is much higher than the remote excitation frequency, we expect that the plasmon frequency downshift results in weaker screening because the polarization charge would not be able to keep up with the time-dependent excitation. In other words, the plasmonic coupling is more strongly affected by *Landau damping*. In simpler remote phonon scattering models,[9–13,22,23] it is not possible to understand the effect of the metal layer on dynamic screening. In our model, plasmonic coupling with the SPPs is explicitly taken into account. Since dynamic screening has been shown to be a consequence of plasmonic coupling, we can model the effect of the top gate on dynamic screening. We find that screening by the top metal gate inhibits electron-electron interaction and consequently reduces the dynamic screening of remote phonon scattering.

In this paper, we demonstrate the advantages of our IPP model by applying it to top-gated SLG. In an earlier paper, we applied the model to the study of gate oxide scaling.[25] The derivation of the model is first presented in some detail in Sec. II. It follows very closely the treatment given in our earlier paper,[19,20] because it is nontrivial to adapt the model to top-gated SLG. In Sec. III, we give the explicit formulas for the electron-IPP coupling coefficient, the transport scattering rate, the electrical conductivity, and the electron mobility. We use the model to study electron transport in a model of top-gated SLG. For simplicity, the SLG is assumed to be supported by a semi-infinite SiO_2 substrate and covered by a HfO_2 top dielectric of finite thickness, similar to that used by Zou *et al.*[24] In Sec. IV, we calculate the electron-SPP and electron-IPP coupling coefficients for different t_{ox} at different electron densities. The t_{ox} scaling of the corresponding SPP-limited and IPP-limited mobility (μ_{SPP} and μ_{IPP}), which give us the upper bound for the total electron mobility, is studied as well. In Sec. V, the electron density dependence of μ_{SPP} and μ_{IPP} is calculated. We also compare our IPP-limited mobility results to the estimates by Zou *et al.*[24] We study the temperature dependence of μ_{IPP} at different electron densities. The contribution of interband transitions to scattering rates and the electron mobility is also quantified. We use our results to illustrate the effect of the top gate on plasmonic coupling and electron momentum relaxation.

II. MODEL OF TOP-GATED SINGLE-LAYER GRAPHENE

The basic model consists of a planar SLG sheet sandwiched between two oxide layers. Let z represent the coordinate along the axis normal to the SLG sheet. The substrate consists of the semi-infinite region $z < 0$ while the top oxide spans the region $h \leqslant z < h + t_{ox}$, where h is the height of the empty space between the two oxide layers, and t_{ox} is the thickness of the top oxide layer. For $z \geqslant h + t_{ox}$, we have a semi-infinite metal layer. Thus all field lines terminate at $z = h + t_{ox}$. For simplicity, we assume that the graphene layer is positioned at the height of $z = d = h/2$, halfway between the oxide layers. The structure is shown in Fig. 1. The top and bottom oxides do not necessarily have to be materially identical although we assume that they each have only two transverse optical (TO) phonon frequencies each. The dielectric response of the bottom and top oxide can be written respectively as

$$\epsilon_{box}(\omega) = \epsilon_{box}^{\infty} + \left(\epsilon_{box}^{0} - \epsilon_{box}^{i}\right)\frac{\omega_{box,T1}^2}{\omega^2 - \omega_{box,T1}^2} + \left(\epsilon_{box}^{i} - \epsilon_{box}^{\infty}\right)\frac{\omega_{box,T2}^2}{\omega^2 - \omega_{box,T2}^2}, \quad (1a)$$

$$\epsilon_{tox}(\omega) = \epsilon_{tox}^{\infty} + \left(\epsilon_{tox}^{0} - \epsilon_{tox}^{i}\right)\frac{\omega_{tox,T1}^2}{\omega^2 - \omega_{tox,T1}^2} + \left(\epsilon_{tox}^{i} - \epsilon_{tox}^{\infty}\right)\frac{\omega_{tox,T2}^2}{\omega^2 - \omega_{tox,T2}^2}, \quad (1b)$$

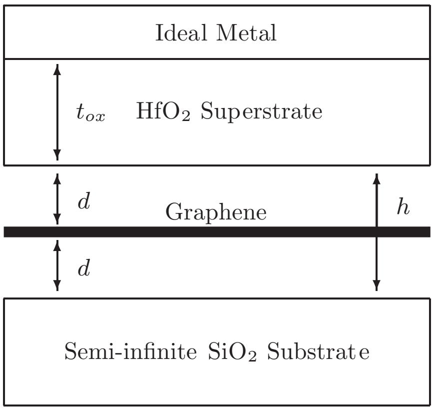

FIG. 1. Basic model used in our calculation. We assume that the graphene is an infinitely thin layer suspended in the middle of the vacuum gap between a semi-infinite bottom oxide layer and a top oxide layer of thickness t_{ox}.

where ϵ_{tox}^{0}, ϵ_{tox}^{i}, and ϵ_{tox}^{∞} (ϵ_{box}^{0}, ϵ_{box}^{i}, and ϵ_{box}^{∞}) are respectively the static, intermediate, and optical permittivity of the top (bottom) oxide layer; $\omega_{tox,T1}$ and $\omega_{tox,T2}$ ($\omega_{box,T1}$ and $\omega_{box,T2}$) are the first and second TO phonon frequency of the top (bottom) oxide layer. More conveniently, the dielectric function for the top and bottom oxide layers can be rewritten in the equivalent generalized Lyddane-Sachs-Teller form[26] as

$$\epsilon_{box}(\omega) = \epsilon_{box}^{\infty}\frac{\left(\omega^2 - \omega_{box,L1}^2\right)\left(\omega^2 - \omega_{box,L2}^2\right)}{\left(\omega^2 - \omega_{box,T1}^2\right)\left(\omega^2 - \omega_{box,T2}^2\right)} \quad (2a)$$

$$\epsilon_{tox}(\omega) = \epsilon_{tox}^{\infty}\frac{\left(\omega^2 - \omega_{tox,L1}^2\right)\left(\omega^2 - \omega_{tox,L2}^2\right)}{\left(\omega^2 - \omega_{tox,T1}^2\right)\left(\omega^2 - \omega_{tox,T2}^2\right)} \quad (2b)$$

where $\omega_{tox,L1}$ and $\omega_{tox,L2}$ ($\omega_{box,L1}$ and $\omega_{box,L2}$) are respectively the first and second longitudinal optical (LO) phonon frequency of the top (bottom) oxide layer, and can be computed from the parameters in Eq. (1).

A. Electrostatic field inside graphene

In this part of the paper, for completeness, we give a brief but detailed derivation of the theory of coupled interfacial plasmon-phonon (IPP) modes in top-gated SLG. A more comprehensive derivation of the general theory can be found in Ref. 19. Nevertheless, sufficient details are provided so that the results of the paper and the model can be replicated.

The Poisson equation for the *screened* scalar potential Φ_{scr} that describes the electrostatic potential between the oxides is

$$-\nabla^2\Phi_{scr}(\mathbf{R},z,t) = \frac{1}{\epsilon_0}\left[\rho_{ox}(\mathbf{R},z,t) + \rho_{scr}(\mathbf{R},z,t)\right], \quad (3)$$

where ρ_{ox} is the (periodic) polarization charge distribution at the surface of the top and bottom oxides that are the source of scattering, ρ_{scr} is the screening charge term inside the graphene, and ϵ_0 is the permittivity of vacuum. The integral form of Eq. (3) is

$$\Phi_{scr}(\mathbf{R},z,t) = \Phi(\mathbf{R},z,t) + \int d\mathbf{R}'dz'G(\mathbf{R}z,\mathbf{R}'z')\rho_{scr}(\mathbf{R}'z',t), \quad (4)$$

where $G(\mathbf{R}z,\mathbf{R}'z')$ is the Green function that satisfies the boundary conditions and the equation

$$-\nabla^2[\epsilon(\mathbf{R},z)G(\mathbf{R}z,\mathbf{R}'z')] = \delta(\mathbf{R}-\mathbf{R}',z-z'). \tag{5}$$

The bare potential $\Phi(\mathbf{R},z,t)$ is defined as $\Phi(\mathbf{R},z,t) = \int d\mathbf{R}'dz'G(\mathbf{R}z,\mathbf{R}'z')\rho_{\text{ox}}(\mathbf{R}'z',t)$. It represents the electrostatic potential in the case where there is no polarization charge. The second term on the right-hand side (RHS) of Eq. (4) represents the screening charge distribution. The bare/screened potential can be written as a sum of its Fourier components:

$$\Phi(\mathbf{R},z,t) = \sum_{\mathbf{Q}} \phi_{Q,\omega}(z)e^{-i\mathbf{Q}\cdot\mathbf{R}}e^{i\omega t}$$

and

$$\Phi_{\text{scr}}(\mathbf{R},z,t) = \sum_{\mathbf{Q}} \phi^{\text{scr}}_{Q,\omega}(z)e^{-i\mathbf{Q}\cdot\mathbf{R}}e^{i\omega t}.$$

We perform the two-dimensional (2D) Fourier transform of Eq. (4). The expression for the z-dependent part of the Fourier-transformed screened potential is

$$\phi^{\text{scr}}_{Q,\omega}(z)e^{i\omega t} = \phi_{Q,\omega}(z)e^{i\omega t} + \int dz' G_Q(z,z')\rho^{\text{scr}}_{Q,\omega}(z',t). \tag{6}$$

Equation (6) is solvable if we express the polarization charge $\rho^{\text{scr}}_{Q,\omega}$ as a function of the screened scalar potential. Here, we write the screening charge term as

$$\rho^{\text{scr}}_{Q,\omega}(z,t) = e^2\Pi(Q,\omega)f(z)\phi^{\text{scr}}_{Q,\omega}(z)e^{i\omega t}, \tag{7}$$

where $\Pi(Q,\omega)$ is the in-plane 2D polarization charge term and $f(z)$ governs the polarization charge distribution in the perpendicular direction. We set $f(z)$ to be normalizable to unity, i.e., $\int dz\, f(z) = 1$. For convenience, we choose $f(z) = \delta(z-d)$. Physically, this implies that we model the graphene as an infinitely thin sheet of polarized charge. Combining Eqs. (6) and (7), we obtain the expression

$$\phi^{\text{scr}}_{Q,\omega}(z) = \phi_{Q,\omega}(z) + e^2\int dz' G_Q(z,z')\Pi(Q,\omega)f(z')\phi^{\text{scr}}_{Q,\omega}(z') \tag{8}$$

which becomes

$$\phi^{\text{scr}}_{Q,\omega}(z) = \phi_{Q,\omega}(z) + \frac{e^2G_Q(z,d)\Pi(Q,\omega)}{1-e^2G_Q(d,d)\Pi(Q,\omega)}\phi_{Q,\omega}(d).$$

The corresponding E field perpendicular to the interface is described by the expression

$$\begin{aligned}\hat{\mathbf{z}}\cdot\mathbf{E}_{Q,\omega} &= -\frac{\partial}{\partial z}\phi^{\text{scr}}_{Q,\omega}(z)\\ &= -\frac{\partial\phi_{Q,\omega}(z,t)}{\partial z} - \frac{\partial G_Q(z,d)}{\partial z}\\ &\quad\times\frac{e^2\Pi(Q,\omega)}{1-e^2G_Q(d,d)\Pi(Q,\omega)}\phi_{Q,\omega}(d).\end{aligned} \tag{9}$$

For notational simplicity, we write

$$\phi^{\text{scr}}_{Q,\omega}(z) = \phi_{Q,\omega}(z) + G_Q(z,d)\mathcal{P}_{Q,\omega}\phi_{Q,\omega}(d), \tag{10a}$$

$$\hat{\mathbf{z}}\cdot\mathbf{E}_{Q,\omega} = -\frac{\partial\phi_{Q,\omega}(z,t)}{\partial z} - \frac{\partial G_Q(z,d)}{\partial z}\mathcal{P}_{Q,\omega}\phi_{Q,\omega}(d), \tag{10b}$$

where $\mathcal{P}_{Q,\omega} = \frac{e^2\Pi(Q,\omega)}{1-e^2G_Q(d,d)\Pi(Q,\omega)}$. Here, we emphasize that Eq. (10a) is the key to determining the dispersion relation as we shall show later.

B. Electrostatic Green function

In order to solve Eq. (10a), we need to have an explicit expression for the electrostatic Green function $G_Q(z,z')$. The Green function contains the details of the electrostatic environment around the graphene sheet.

The Green function $G_Q(z,z')$ for a source in the empty space between the top and bottom oxide layers ($0 < z' \leqslant h$) satisfies

$$-\left(\frac{\partial^2}{\partial z^2} - Q^2\right)G_Q(z,z') = \frac{1}{\epsilon_0}\delta(z-z').$$

This implies that we can always express $G_Q(z,z')$ as a linear combination of e^{Qz} and e^{-Qz}, or $\cosh(Qz)$ and $\sinh(Qz)$. Following Eq. (1), we define the optical permittivity of the top and bottom oxide layers to be $\epsilon^{\infty}_{\text{tox}}$ and $\epsilon^{\infty}_{\text{box}}$, respectively. The Green function has to satisfy the following continuity conditions at the interfaces $z = 0$, $z = h$, and $z = h + t_{\text{ox}}$:

$$G_Q(h+t_{ox},z') = \lim_{z\to-\infty} G_Q(z,z') = 0, \tag{11a}$$

$$G_Q(h^+,z') = G_Q(h^-,z'), \tag{11b}$$

$$G_Q(0^+,z') = G_Q(0^-,z'), \tag{11c}$$

$$\epsilon^{\infty}_{\text{tox}}\frac{\partial G_Q(z=h^+,z')}{\partial z} = \epsilon_0\frac{\partial G_Q(z=h^-,z')}{\partial z}, \tag{11d}$$

$$\epsilon_0\frac{\partial G_Q(z=0^+,z')}{\partial z} = \epsilon^{\infty}_{\text{box}}\frac{\partial G_Q(z=0^-,z')}{\partial z}. \tag{11e}$$

We use the optical permittivities ($\epsilon^{\infty}_{\text{tox}}$ and $\epsilon^{\infty}_{\text{box}}$) in Eqs. (11d) and (11e) instead of the frequency-dependent permittivities [$\epsilon_{\text{tox}}(\omega)$ and $\epsilon_{\text{box}}(\omega)$] because the use of the latter would result in the *decoupling* of the SPP modes to the plasmons when we compute the plasmon-phonon dispersion later.

The expression for $G_Q(0 < z \leqslant h, 0 < z' \leqslant h)$ that satisfies these continuity conditions is

$$\begin{aligned}G_Q(z,z') = \frac{1}{2\epsilon_0 Q}\Bigg\{& e^{-Q|z-z'|} + \frac{\lambda_t\lambda_b e^{-2Qh}}{1-\lambda_t\lambda_b e^{-2Qh}}\\ &\times[e^{-Q(z-z')} + e^{Q(z-z')}] - \frac{1}{1-\lambda_t\lambda_b e^{-2Qh}}\\ &\times[\lambda_t e^{Q(z+z'-2h)} + \lambda_b e^{-Q(z+z')}]\Bigg\},\end{aligned} \tag{12}$$

where

$$\lambda_t = \frac{\epsilon^{\infty}_{\text{tox}}\coth Qt_{\text{ox}} - \epsilon_0}{\epsilon^{\infty}_{\text{tox}}\coth Qt_{\text{ox}} + \epsilon_0}, \quad \lambda_b = \frac{\epsilon^{\infty}_{\text{box}} - \epsilon_0}{\epsilon^{\infty}_{\text{box}} + \epsilon_0}.$$

The permittivity constants in Eq. (12) correspond to the optical ($\epsilon^{\infty}_{\text{box}}$ and $\epsilon^{\infty}_{\text{tox}}$), and not the static, dielectric response ($\epsilon^{0}_{\text{box}}$ and $\epsilon^{0}_{\text{tox}}$). In the region $h \leqslant z < h + t_{\text{ox}}$, making use of the continuity of the Green function and the fact that it has to terminate at $z = h + t_{\text{ox}}$, we can easily write the Green function as

$$G_Q(z > h,z') = G(h,z')\frac{\sinh Q(h+t_{\text{ox}}-z)}{\sinh Qt_{\text{ox}}}$$

and likewise, for $z < 0$, the Green function is

$$G_Q(z < 0,z') = G(0,z')e^{+Qz}.$$

C. Scattering field

The *bare* scalar potential $\phi_{Q,\omega}(z)$ has to satisfy the equation

$$\left(\frac{d^2}{dz^2} - Q^2\right)\phi_{Q,\omega}(z) = 0.$$

This implies that $\phi_{Q,\omega}$ can be written as a linear combination of e^{+Qz} and e^{-Qz}. At the interfaces $z = h$ and $z = 0$, we require the continuity of $\phi_{Q,\omega}$, i.e.,

$$\phi_{Q,\omega}(h^+) = \phi_{Q,\omega}(h^-)$$

and

$$\phi_{Q,\omega}(0^+) = \phi_{Q,\omega}(0^-).$$

We also require that

$$\lim_{z\to-\infty} \phi_{Q,\omega}(z) = \phi_{Q,\omega}(h + t_{\rm ox}) = 0.$$

This suggests that we can write $\phi_{Q,\omega}(z)$ in a symmetric way:

$$\phi_{Q,\omega}(z) = \begin{cases} (Ae^{-Qh} + B)\frac{\sinh Q(h+t_{\rm ox}-z)}{\sinh Qt_{\rm ox}}, & h < z \leqslant h + t_{\rm ox}, \\ Ae^{-Qz} + Be^{+Q(z-h)}, & 0 < z \leqslant h, \\ (A + Be^{-Qh})e^{+Qz}, & z \leqslant 0, \end{cases}$$

where A and B are independent variables. Thus the screened potential $\phi^{\rm scr}_{Q,\omega}(z)$ is, according to Eq. (10a),

$$\phi^{\rm scr}_{Q,\omega}(z) = \begin{cases} (Ae^{-Qh} + B)\frac{\sinh Q(h+t_{\rm ox}-z)}{\sinh Qt_{\rm ox}} + G_Q(z,d)\mathcal{P}_{Q,\omega}\,(A + B)\,e^{-Qd}, & h < z \leqslant h + t_{\rm ox}, \\ Ae^{-Qz} + Be^{+Q(z-h)} + G_Q(z,d)\mathcal{P}_{Q,\omega}\,(A + B)\,e^{-Qd}, & 0 < z \leqslant h, \\ (A + Be^{-Qh})e^{+Qz} + G_Q(z,d)\mathcal{P}_{Q,\omega}\,(A + B)\,e^{-Qd}, & z \leqslant 0. \end{cases} \tag{13}$$

The coefficients A and B can be regarded as the amplitude of the scattering fields localized at $z = 0$ and $z = h$, respectively. In general, they are functions of Q and ω, with ω determined by the boundary conditions,

$$\epsilon_{\rm tox}(\omega)\frac{\partial\phi^{\rm scr}_{Q,\omega}(z = h^+)}{\partial z} = \epsilon_0\frac{\partial\phi^{\rm scr}_{Q,\omega}(z = h^-)}{\partial z}, \tag{14a}$$

$$\epsilon_0\frac{\partial\phi^{\rm scr}_{Q,\omega}(z = 0^+)}{\partial z} = \epsilon_{\rm box}(\omega)\frac{\partial\phi^{\rm scr}_{Q,\omega}(z = 0^-)}{\partial z}. \tag{14b}$$

If we make use of the relations $G_Q(z > h,d) = G_Q(h,d)\frac{\sinh Q(h+t_{ox}-z)}{\sinh Qt_{ox}}$ and $G_Q(z < 0,d) = G_Q(0,d)e^{+Qz}$, then Eq. (13) can be written as

$$\phi^{\rm scr}_{Q,\omega}(z) = \begin{cases} [Ae^{-Qh} + B + G_Q(h,d)\mathcal{P}_{Q,\omega}\,(A + B)\,e^{-Qd}]\frac{\sinh Q(h+t_{\rm ox}-z)}{\sinh Qt_{\rm ox}}, & h < z \leqslant h + t_{\rm ox}, \\ Ae^{-Qz} + Be^{+Q(z-h)} + G_Q(z,d)\mathcal{P}_{Q,\omega}\,(A + B)\,e^{-Qd}, & 0 < z \leqslant h, \\ [A + Be^{-Qh} + G_Q(0,d)\mathcal{P}_{Q,\omega}\,(A + B)\,e^{-Qd}]e^{+Qz}, & z \leqslant 0. \end{cases}$$

The derivative of $\phi^{\rm scr}_{Q,\omega}(z)$ is

$$\frac{d\phi^{\rm scr}_{Q,\omega}(z)}{dz} = \begin{cases} -Q[Ae^{-Qh} + B + G_Q(h,d)\mathcal{P}_{Q,\omega}\,(A + B)\,e^{-Qd}]\frac{\cosh Q(h+t_{\rm ox}-z)}{\sinh Qt_{\rm ox}}, & h < z \leqslant h + t_{\rm ox}, \\ Q[-Ae^{-Qz} + Be^{+Q(z-h)}] + \frac{\partial}{\partial z}G_Q(z,d)\mathcal{P}_{Q,\omega}\,(A + B)\,e^{-Qd}, & 0 < z \leqslant h, \\ +Q[A + Be^{-Qh} + G_Q(0,d)\mathcal{P}_{Q,\omega}\,(A + B)\,e^{-Qd}]e^{+Qz}, & z \leqslant 0. \end{cases}$$

From the continuity of $\epsilon(z)\frac{d}{dz}\phi^{\rm scr}_{Q,\omega}(z)$ at $z = h$, we obtain the equation

$$\begin{aligned} &-\epsilon_{\rm tox}(\omega)\coth(Qt_{\rm ox})Q[Ae^{-Qh} + B + G_Q(h,d)\mathcal{P}_{Q,\omega}\,(A + B)\,e^{-Qd}] \\ &= \epsilon_0 Q(-Ae^{-Qh} + B) + \epsilon_0\frac{\partial}{\partial z}G_Q(z = h^-,d)\mathcal{P}_{Q,\omega}\,(A + B)\,e^{-Qd} \\ &= Q[\epsilon_0(-Ae^{-Qh} + B) - \epsilon^\infty_{\rm tox}\coth(Qt_{\rm ox})G_Q(h,d)\mathcal{P}_{Q,\omega}\,(A + B)\,e^{-Qd}] \end{aligned}$$

or, as a linear combination of A and B,

$$\begin{aligned} &\left\{[\epsilon_{\rm tox}(\omega)\coth(Qt_{\rm ox}) - \epsilon_0]e^{-Qh} + \left[\epsilon_{\rm tox}(\omega) - \epsilon^\infty_{\rm tox}\right]\coth(Qt_{\rm ox})G_Q(h,d)\mathcal{P}_{Q,\omega}e^{-Qd}\right\}A \\ &+ \left\{[\epsilon_{\rm tox}(\omega)\coth(Qt_{\rm ox}) + \epsilon_0] + \left[\epsilon_{\rm tox}(\omega) - \epsilon^\infty_{\rm tox}\right]\coth(Qt_{\rm ox})G_Q(h,d)\mathcal{P}_{Q,\omega}e^{-Qd}\right\}B = 0. \end{aligned} \tag{15}$$

Similarly, at $z = 0$, we have

$$\left\{[\epsilon_{\text{box}}(\omega) - \epsilon_0]\, e^{-Qh} + \left[\epsilon_{\text{box}}(\omega) - \epsilon_{\text{box}}^{\infty}\right] G_Q(0,d)\mathcal{P}_{Q,\omega}e^{-Qd}\right\} B + \left\{[\epsilon_{\text{box}}(\omega) + \epsilon_0] + \left[\epsilon_{\text{box}}(\omega) - \epsilon_{\text{box}}^{\infty}\right] G_Q(0,d)\mathcal{P}_{Q,\omega}e^{-Qd}\right\} A = 0. \tag{16}$$

After combining Eqs. (15) and (16) into a matrix equation, we obtain the corresponding secular equation

$$\begin{aligned} &\left\{ [\epsilon_{\text{box}}(\omega) + \epsilon_0] + \left[\epsilon_{\text{box}}(\omega) - \epsilon_{\text{box}}^{\infty}\right] G_Q(0,d)\mathcal{P}_{Q,\omega}e^{-Qd}\right\} \\ &\quad \times \left\{ [\epsilon_{\text{tox}}(\omega)\coth(Qt_{\text{ox}}) + \epsilon_0] + \left[\epsilon_{\text{tox}}(\omega) - \epsilon_{\text{tox}}^{\infty}\right] \coth(Qt_{\text{ox}}) G_Q(h,d)\mathcal{P}_{Q,\omega}e^{-Qd}\right\} \\ &\quad - \left\{ [\epsilon_{\text{box}}(\omega) - \epsilon_0]\, e^{-Qh} + \left[\epsilon_{\text{box}}(\omega) - \epsilon_{\text{box}}^{\infty}\right] G_Q(0,d)\mathcal{P}_{Q,\omega}e^{-Qd}\right\} \\ &\quad \times \left\{ [\epsilon_{\text{tox}}(\omega)\coth(Qt_{\text{ox}}) - \epsilon_0]\, e^{-Qh} + \left[\epsilon_{\text{tox}}(\omega) - \epsilon_{\text{tox}}^{\infty}\right] \coth(Qt_{\text{ox}}) G_Q(h,d)\mathcal{P}_{Q,\omega}e^{-Qd}\right\} = 0 \end{aligned} \tag{17}$$

from the determinant of the matrix. Solving Eq. (17) for each value of Q yields a set of five corresponding ω_Q values ($\omega_Q^{(\text{IPP1})}$, $\omega_Q^{(\text{IPP2})}$, $\omega_Q^{(\text{IPP3})}$, $\omega_Q^{(\text{IPP4})}$, and $\omega_Q^{(\text{IPP5})}$), assuming that $\Pi(Q,\omega) \propto 1/\omega^2$. Once these ω_Q values are found, the ratio of A to B can be fixed. If we ignore the top oxide layer and set $\epsilon_{\text{tox}}(\omega) = \epsilon_0$, then we obtain the secular equation for the bottom oxide layer, i.e.,

$$[\epsilon_{\text{box}}(\omega) + \epsilon_0] + \left[\epsilon_{\text{box}}(\omega) - \epsilon_{\text{box}}^{\infty}\right] G_Q(0,d)\mathcal{P}_{Q,\omega}e^{-Qd} = 0. \tag{18}$$

Here, our decision to not use $\epsilon_{\text{tox}}(\omega)$ and $\epsilon_{\text{box}}(\omega)$ in Eqs. (11d) and (11e) can be justified. Take the simple case where we have only the bottom oxide layer. Suppose we had used $\epsilon_{\text{box}}(\omega)$ instead of $\epsilon_{\text{box}}^{\infty}$ in Eq. (11e). Then the dispersion relation for the coupled phonon-plasmon modes would be

$$\epsilon_{\text{box}}(\omega) + \epsilon_0 = 0 \tag{19}$$

instead of Eq. (18). The dispersion relation in Eq. (19) is unphysical as it is independent of the plasmon dispersion.

Equation (17) can be simplified considerably if we set $h = 2d = 0$, i.e., the gap size is zero. The simplified version of Eq. (17) is

$$\epsilon_{\text{box}}(\omega) + \epsilon_{\text{tox}}(\omega)\coth(Qt_{\text{ox}}) - \frac{e^2\Pi(Q,\omega)}{Q}. \tag{20}$$

The second and third term in Eq. (20) can be interpreted as the dielectric response of the top gate-plasmon composite system.

D. Scattering amplitude

To determine the scattering amplitude of the effective scattering potential, we use the approach developed in Ref. 26, in which the time-averaged total energy $\langle \mathcal{W}_{Q,\omega}\rangle$ (the brackets $\langle\cdots\rangle$ denote time average) associated with a coupled phonon-plasmon mode is set equal to its zero-point energy. The time-averaged total energy is simply twice the time-averaged potential energy $\langle \mathcal{U}_{Q,\omega}^{\text{scr}}\rangle$, which can be evaluated from the volume integral of $\frac{1}{2}\mathbf{D}\cdot\mathbf{E}$, with $\mathbf{D}$ and $\mathbf{E}$ equal to the electric displacement and field, respectively.

In determining $\langle \mathcal{U}_{Q,\omega}^{\text{scr}}\rangle$, we will not evaluate the volume integral of $\frac{1}{2}\mathbf{D}\cdot\mathbf{E}$ but simply take the sum of the product of the surface charge density and the potential at the two interfaces. Consideration of the charge density on the graphene is excised from our calculation. The time-averaged potential energy can be written as

$$\left\langle \mathcal{U}_{Q,\omega}^{\text{scr}}\right\rangle = \left\langle \mathcal{U}_{Q,\omega}^{\text{scr}}(z=0)\right\rangle + \left\langle \mathcal{U}_{Q,\omega}^{\text{scr}}(z=h)\right\rangle,$$

where

$$\begin{aligned} &\left\langle \mathcal{U}_{Q,\omega}^{\text{scr}}(z=h)\right\rangle \\ &\quad = \left\langle -\frac{1}{2}\Omega\left[\bar{\epsilon}_{\text{tox}}(\omega)\frac{\partial\phi_{Q,\omega}(z=h^+)}{\partial z} \right.\right. \\ &\qquad \left.\left. - \epsilon_0\frac{\partial\phi_{Q,\omega}(z=h^-)}{\partial z}\right]\phi_{Q,\omega}^{\text{scr}}(z=h)\right\rangle \end{aligned} \tag{21}$$

is the contribution from the top interface and

$$\begin{aligned} &\left\langle \mathcal{U}_{Q,\omega}^{\text{scr}}(z=0)\right\rangle \\ &\quad = \left\langle -\frac{1}{2}\Omega\left[\bar{\epsilon}_{\text{box}}(\omega)\frac{\partial\phi_{Q,\omega}(z=0^+)}{\partial z} \right.\right. \\ &\qquad \left.\left. - \epsilon_0\frac{\partial\phi_{Q,\omega}(z=h^-)}{\partial z}\right]\phi_{Q,\omega}^{\text{scr}}(z=0)\right\rangle \end{aligned} \tag{22}$$

is the contribution from the bottom interface; Ω is the area of the interface. The term $\bar{\epsilon}_{\text{box}}(\omega)$ is not the dielectric function of the bottom oxide but a distinct variable from $\epsilon_{\text{box}}(\omega)$. The same is true of $\bar{\epsilon}_{\text{tox}}(\omega)$ and $\epsilon_{\text{tox}}(\omega)$. The former can be modified to contain the response of a specific excitation. Recall from Eq. (2) that we can write the dielectric function in the LST form:

$$\epsilon_{\text{box}}(\omega) = \epsilon_{\text{box}}^{\infty}\kappa_{\text{box}}^{(1)}(\omega)\kappa_{\text{box}}^{(2)}(\omega)$$

where the function

$$\kappa_{\text{box}}^{(m)}(\omega) = \frac{\omega^2 - \omega_{\text{box},Lm}^2}{\omega^2 - \omega_{\text{box},Tm}^2}$$

for $m = 1,2$ describes the dielectric response of the phonon in the bottom oxide. The dielectric function for the top oxide can be similarly written as $\epsilon_{\text{tox}}(\omega) = \epsilon_{\text{tox}}^{\infty}\kappa_{\text{tox}}^{(1)}(\omega)\kappa_{\text{tox}}^{(2)}(\omega)$. To isolate the optical dielectric response of the bottom oxide phonon 1 at frequency ω, we set

$$\bar{\epsilon}_{\text{box}}(\omega) = \bar{\epsilon}_{\text{box}}^{\text{HI},1}(\omega) \equiv \epsilon_{\text{box}}^{\infty}\kappa_{\text{box}}^{(1)}(\infty)\kappa_{\text{box}}^{(2)}(\omega), \tag{23}$$

while to isolate the corresponding static dielectric response, we set

$$\overline{\epsilon}_{\text{box}}(\omega) = \overline{\epsilon}_{\text{box}}^{\text{LO},1}(\omega) \equiv \epsilon_{\text{box}}^{\infty}\kappa_{\text{box}}^{(1)}(0)\kappa_{\text{box}}^{(2)}(\omega)\ . \tag{24}$$

The optical and static dielectric responses of the bottom oxide phonon 2 and the top oxide phonons can be similarly defined.

The explicit expression for Eq. (21) is

$$\begin{aligned}\left\langle \mathcal{U}_{Q,\omega}^{\text{scr}}(z=h)\right\rangle = \frac{1}{2}\Omega Q\Big\{\big\{\,[\overline{\epsilon}_{\text{tox}}(\omega)\coth(Qt_{\text{ox}}) - \epsilon_0]\,e^{-Qh} + \big[\overline{\epsilon}_{\text{tox}}(\omega) - \epsilon_{\text{tox}}^{\infty}\big]\coth(Qt_{\text{ox}})G_Q(h,d)\mathcal{P}_{Q,\omega}e^{-Qd}\big\}A \\ + \big\{\,[\overline{\epsilon}_{\text{tox}}(\omega)\coth(Qt_{\text{ox}}) + \epsilon_0] + \big[\overline{\epsilon}_{\text{tox}}(\omega) - \epsilon_{\text{tox}}^{\infty}\big]\coth(Qt_{\text{ox}})G_Q(h,d)\mathcal{P}_{Q,\omega}e^{-Qd}\big\}B\Big\} \\ \times [Ae^{-Qh} + B + G_Q(h,d)\mathcal{P}_{Q,\omega}\,(A+B)\,e^{-Qd}].\end{aligned}$$

Using Eq. (15), the above expression becomes

$$\left\langle \mathcal{U}_{Q,\omega}^{\text{scr}}(z=h)\right\rangle = \tfrac{1}{2}\Omega Q\,[\overline{\epsilon}_{\text{tox}}(\omega) - \epsilon_{\text{tox}}(\omega)]\coth(Qt_{\text{ox}})[Ae^{-Qh} + B + G_Q(h,d)\mathcal{P}_{Q,\omega}\,(A+B)\,e^{-Qd}]^2. \tag{25}$$

Similarly, using Eq. (16), the explicit expression for Eq. (22) is

$$\left\langle \mathcal{U}_{Q,\omega}^{\text{scr}}(z=0)\right\rangle = \tfrac{1}{2}\Omega Q[\overline{\epsilon}_{\text{box}}(\omega) - \epsilon_{\text{box}}(\omega)][A + Be^{-Qh} + G_Q(0,d)\mathcal{P}_{Q,\omega}\,(A+B)\,e^{-Qd}]^2. \tag{26}$$

Once the secular equation (17) has been solved, the variables A and B are no longer independent. Hence, for each set of values of Q and $\omega = \omega_Q$, using Eq. (15) or (16), we can set $B = \alpha_{Q,\omega}A$, where

$$\begin{aligned}\alpha_{Q,\omega} &= -\frac{[\epsilon_{\text{tox}}(\omega)\coth(Qt_{\text{ox}}) - \epsilon_0]\,e^{-Qh} + \big[\epsilon_{\text{tox}}(\omega) - \epsilon_{\text{tox}}^{\infty}\big]\coth(Qt_{\text{ox}})G_Q(h,d)\mathcal{P}_{Q,\omega}e^{-Qd}}{[\epsilon_{\text{tox}}(\omega)\coth(Qt_{\text{ox}}) + \epsilon_0] + \big[\epsilon_{\text{tox}}(\omega) - \epsilon_{\text{tox}}^{\infty}\big]\coth(Qt_{\text{ox}})G_Q(h,d)\mathcal{P}_{Q,\omega}e^{-Qd}} \\ &= -\frac{[\epsilon_{\text{box}}(\omega) + \epsilon_0] + \big[\epsilon_{\text{box}}(\omega) - \epsilon_{\text{box}}^{\infty}\big]\,G_Q(0,d)\mathcal{P}_{Q,\omega}e^{-Qd}}{[\epsilon_{\text{box}}(\omega) - \epsilon_0]\,e^{-Qh} + \big[\epsilon_{\text{box}}(\omega) - \epsilon_{\text{box}}^{\infty}\big]\,G_Q(0,d)\mathcal{P}_{Q,\omega}e^{-Qd}}.\end{aligned}$$

Note that if we set $\epsilon_{\text{tox}}(\omega) = \epsilon_{\text{tox}}^{\infty} = \epsilon_0$, then $\alpha_{Q,\omega} = 0$ as it should be since we expect B (the amplitude of the field localized at the top interface) to equal zero in the absence of a top oxide layer. Thus B can be eliminated from Eqs. (25) and (26), and we obtain

$$\left\langle \mathcal{U}_{Q,\omega}^{\text{scr}}(z=h)\right\rangle = \tfrac{1}{2}\Omega Q[\overline{\epsilon}_{\text{tox}}(\omega) - \epsilon_{\text{tox}}(\omega)]\coth(Qt_{\text{ox}})[e^{-Qh} + \alpha_{Q,\omega} + G_Q(h,d)\mathcal{P}_{Q,\omega}(1+\alpha_{Q,\omega})e^{-Qd}]^2A^2 \tag{27}$$

and

$$\left\langle \mathcal{U}_{Q,\omega}^{\text{scr}}(z=0)\right\rangle = \tfrac{1}{2}\Omega Q[\overline{\epsilon}_{\text{box}}(\omega) - \epsilon_{\text{box}}(\omega)][e^{-Qh} + \alpha_{Q,\omega} + G_Q(0,d)\mathcal{P}_{Q,\omega}(A+B)e^{-Qd}]^2A^2. \tag{28}$$

There is a convenient interpretation of the square-bracketed factors on the RHS of Eqs. (27) and (28). The first $[\cdots]$ is the coupling strength determined by the polarization charges in the top/bottom oxide; the second $[\cdots]$ is related to the electrostatics and geometry of the system. Next, to find the expression for A, we assume $\langle \mathcal{W}_{Q,\omega}\rangle = 2\langle \mathcal{U}_{Q,\omega}^{\text{scr}}\rangle$, which relates the time-averaged total energy to the time-averaged potential energy, to obtain

$$\begin{aligned}\langle \mathcal{W}_{Q,\omega}\rangle = \Omega QA^2\{[\overline{\epsilon}_{\text{tox}}(\omega) - \epsilon_{\text{tox}}(\omega)]\coth(Qt_{\text{ox}})[e^{-Qh} + \alpha_{Q,\omega} + G_Q(h,d)\mathcal{P}_{Q,\omega}(1+\alpha_{Q,\omega})e^{-Qd}]^2 \\ + [\overline{\epsilon}_{\text{box}}(\omega) - \epsilon_{\text{box}}(\omega)][e^{-Qh} + \alpha_{Q,\omega} + G_Q(0,d)\mathcal{P}_{Q,\omega}(1+\alpha_{Q,\omega})e^{-Qd}]^2\}.\end{aligned}$$

From the zero-point relation $\langle \mathcal{W}_{Q,\omega}\rangle = \frac{1}{2}\hbar\omega_Q$, the expression for the amplitude can be determined:

$$\begin{aligned}A^2 = \frac{\hbar\omega_Q}{2\Omega Q}\{[\overline{\epsilon}_{\text{tox}}(\omega) - \epsilon_{\text{tox}}(\omega)]\coth(Qt_{\text{ox}})[e^{-Qh} + \alpha_{Q,\omega} + G_Q(h,d)\mathcal{P}_{Q,\omega}(1+\alpha_{Q,\omega})e^{-Qd}]^2 \\ + [\overline{\epsilon}_{\text{box}}(\omega) - \epsilon_{\text{box}}(\omega)][e^{-Qh} + \alpha_{Q,\omega} + G_Q(0,d)\mathcal{P}_{Q,\omega}(1+\alpha_{Q,\omega})e^{-Qd}]^2\}^{-1}.\end{aligned}$$

Hence, by taking the square amplitude difference between the optical and static dielectric response, the scattering potential $\phi_{Q,\omega}^{\text{scr}}(d) = [1 + G_Q(d,d)\mathcal{P}_{Q,\omega}]\,(A+B)\,e^{-Qd}$ can be expressed, say for the top oxide phonon mode 1, as

$$\phi_{Q,\omega}^{\text{scr}}(d) = \left[\frac{\hbar\omega_Q}{2\Omega Q}\left(\frac{1}{\overline{\epsilon}_{\text{tox}}^{\text{HI},1}(\omega) - \epsilon_{\text{tox}}(\omega)} - \frac{1}{\overline{\epsilon}_{\text{tox}}^{\text{LO},1}(\omega) - \epsilon_{\text{tox}}(\omega)}\right)\right]^{\frac{1}{2}}\mathcal{F}_{Q,\omega}^{(\text{top})}, \tag{29}$$

where $\overline{\epsilon}_{\text{tox}}^{\text{HI},1}(\omega)$ and $\overline{\epsilon}_{\text{tox}}^{\text{LO},1}(\omega)$ are defined as in Eqs. (23) and (24), and

$$\begin{aligned}\mathcal{F}_{Q,\omega}^{(\text{top})} &= \frac{[1 + G_Q(d,d)\mathcal{P}_{Q,\omega}](1+\alpha_{Q,\omega})e^{-Qd}}{e^{-Qh} + \alpha_{Q,\omega} + G_Q(h,d)\mathcal{P}_{Q,\omega}(1+\alpha_{Q,\omega})e^{-Qd}}\left[\frac{1}{\coth(Qt_{\text{ox}})}\right]^{1/2} \\ &= \frac{(1+\alpha_{Q,\omega})e^{-Qd}}{(e^{-Qh} + \alpha_{Q,\omega})[1 - G_Q(d,d)e^2\Pi(Q,\omega)] + G_Q(h,d)e^2\Pi(Q,\omega)(1+\alpha_{Q,\omega})e^{-Qd}}\left[\frac{1}{\coth(Qt_{\text{ox}})}\right]^{1/2}.\end{aligned}$$

Similarly, for the bottom oxide phonon mode 1,

$$\phi^{\mathrm{scr}}_{Q,\omega}(d) = \left[\frac{\hbar\omega_Q}{2\Omega Q}\left(\frac{1}{\overline{\epsilon}^{\mathrm{HI},1}_{\mathrm{box}}(\omega) - \epsilon_{\mathrm{box}}(\omega)} - \frac{1}{\overline{\epsilon}^{\mathrm{LO},1}_{\mathrm{box}}(\omega) - \epsilon_{\mathrm{box}}(\omega)}\right)\right]^{\frac{1}{2}} \mathcal{F}^{(\mathrm{bot})}_{Q,\omega},$$

where

$$\begin{aligned}\mathcal{F}^{(\mathrm{bot})}_{Q,\omega} &= \frac{[1 + G_Q(d,d)\mathcal{P}_{Q,\omega}](1+\alpha_{Q,\omega})e^{-Qd}}{1 + \alpha_{Q,\omega}e^{-Qh} + G_Q(0,d)\mathcal{P}_{Q,\omega}(1+\alpha_{Q,\omega})e^{-Qd}} \\ &= \frac{(1+\alpha_{Q,\omega})e^{-Qd}}{(1+\alpha_{Q,\omega}e^{-Qh})[1 - G_Q(d,d)e^2\Pi(Q,\omega)] + G_Q(0,d)e^2\Pi(Q,\omega)(1+\alpha_{Q,\omega})e^{-Qd}}.\end{aligned}$$

In the long wavelength limit ($Q \to 0$), we have $\mathcal{F}^{(\mathrm{top})}_{Q,\omega} \to 1$ and $\mathcal{F}^{(\mathrm{bot})}_{Q,\omega} \to 1$.

If we set the graphene-oxide gap equal to zero (i.e., $h = 2d = 0$), $\mathcal{F}^{(\mathrm{top})}_{Q,\omega}$ and $\mathcal{F}^{(\mathrm{bot})}_{Q,\omega}$ also simplify to $\mathcal{F}^{(\mathrm{top})}_{Q,\omega} = [\coth(Qt_{\mathrm{ox}})]^{-1/2}$ and $\mathcal{F}^{(\mathrm{bot})}_{Q,\omega} = 1$, respectively. The scattering potential for the top oxide phonon mode 1 in Eq. (29) also becomes

$$\phi^{\mathrm{scr}}_{Q,\omega} = \left[\frac{\hbar\omega}{2\Omega Q}\left(\frac{1}{\overline{\epsilon}^{\mathrm{HI},1}_{\mathrm{tox}}(\omega)\coth(Qt_{\mathrm{ox}}) + \epsilon_{\mathrm{box}}(\omega) - \frac{e^2}{Q}\Pi(Q,\omega)} - \frac{1}{\overline{\epsilon}^{\mathrm{LO},1}_{\mathrm{tox}}(\omega)\coth(Qt_{\mathrm{ox}}) + \epsilon_{\mathrm{box}}(\omega) - \frac{e^2}{Q}\Pi(Q,\omega)}\right)\right]^{\frac{1}{2}}. \quad (30)$$

Likewise, the scattering potential for the bottom oxide phonon mode 1 is

$$\phi^{\mathrm{scr}}_{Q,\omega} = \left[\frac{\hbar\omega}{2\Omega Q}\left(\frac{1}{\epsilon_{\mathrm{tox}}(\omega)\coth(Qt_{\mathrm{ox}}) + \overline{\epsilon}^{\mathrm{HI},1}_{\mathrm{box}}(\omega) - \frac{e^2}{Q}\Pi(Q,\omega)} - \frac{1}{\epsilon_{\mathrm{tox}}(\omega)\coth(Qt_{\mathrm{ox}}) + \overline{\epsilon}^{\mathrm{LO},1}_{\mathrm{box}}(\omega) - \frac{e^2}{Q}\Pi(Q,\omega)}\right)\right]^{\frac{1}{2}}. \quad (31)$$

The expression in Eqs. (30) and (31) is analogous to the one derived by Wang and Mahan[27] for surface potential scattering of electrons, which is

$$\phi_{Q,\omega} = \left[\frac{\hbar\omega}{2\Omega Q}\left(\frac{1}{\epsilon_{\mathrm{box}}(\infty) + \epsilon_0} - \frac{1}{\epsilon_{\mathrm{box}}(0) + \epsilon_0}\right)\right]^{\frac{1}{2}}. \quad (32)$$

The expression by Wang and Mahan in Eq. (32) is simpler than ours because there are no plasmons and top gate in their model. Nonetheless, the strong analogy between our expression and theirs supports the soundness of our derivation.

E. Phonon content

From Eq. (17), we can determine five values of ω for each value of $\mathbf{Q}$. Thus, in the IPP dispersion relation, there are five distinct branches ($\omega_Q^{(i)}$, $i = \mathrm{IPP}_1$ to IPP_5). Each branch represents excitations of the *coupled* phonon-plasmon system. However, the *effective* scattering amplitude of a particular mode may not be significant if it is plasmonlike. Scattering with a plasmonlike excitation does not necessarily lead to the loss of momentum since the momentum is simply transferred to the constituent electrons of the plasmon excitation and there is no change in the total momentum of all the electrons. On the other hand, scattering with a phononlike excitation can lead to the loss of momentum since phonons belong to a different set of degrees of freedom.

Therefore, as in Refs. 26 and 19, it is necessary to define the *phonon content* of each mode. In the uncoupled system, there are four SPP phonon branches ($\omega_Q^{(\mathrm{SPP1})}$, $\omega_Q^{(\mathrm{SPP2})}$, $\omega_Q^{(\mathrm{SPP3})}$, and $\omega_Q^{(\mathrm{SPP4})}$)—two from the top oxide and two from the bottom. We enumerate the former pair $\omega_Q^{(-g,1)} = \omega_{\mathrm{tox},S1}(Q)$ and $\omega_Q^{(-g,2)} = \omega_{\mathrm{tox},S2}(Q)$, and the latter pair $\omega_Q^{(-g,3)} = \omega_{\mathrm{box},S1}(Q)$ and $\omega_Q^{(-g,4)} = \omega_{\mathrm{box},S2}(Q)$. They can be computed from Eq. (17) but with e^2 set to zero, i.e.,

$$\begin{aligned}&[\epsilon_{\mathrm{box}}(\omega) + \epsilon_0]\,[\epsilon_{\mathrm{tox}}(\omega)\coth(Qt_{\mathrm{ox}}) + \epsilon_0] \\ &\quad - [\epsilon_{\mathrm{box}}(\omega) - \epsilon_0]\,[\epsilon_{\mathrm{tox}}(\omega)\coth(Qt_{\mathrm{ox}}) - \epsilon_0]\,e^{-2Qh} = 0. \quad (33)\end{aligned}$$

First of all, we determine the plasmon content of each IPP mode $\omega_Q^{(i)}$. As in Ref. 19, this is accomplished by setting

$$\Phi^{(g)}(\omega_Q^{(i)}) = \left|\frac{\Pi_{n=1}^{4}\left(\omega_Q^{(i)2} - \omega_Q^{(-g,n)2}\right)}{\Pi_{j=1,i\neq j}^{5}\left(\omega_Q^{(i)2} - \omega_Q^{(j)2}\right)}\right|. \quad (34)$$

The numerator and denominator in Eq. (34) are quartic in ω^2. The expression in Eq. (34) approaches zero (unity) whenever $\omega_Q^{(i)}$ moves towards (away from) one of the SPP frequencies. Note that the expected "sum rule,"[26]

$$\sum_{i=1}^{5}\Phi^{(g)}\left(\omega_Q^{(i)}\right) = 1, \quad (35)$$

holds for each value of $\mathbf{Q}$. Equation (35) implies that the total plasmon weight of the given solutions is equal to one (as it would be without hybridization). The (nonplasmon) phonon content is then defined as $1 - \Phi^{(g)}(\omega_Q^{(i)})$. In order to distinguish the phonon parts of the nonplasmon content, we need to define the relative individual phonon content. For top oxide TO1 phonon, the content is computed by ignoring its response and replacing $\epsilon_{\mathrm{tox}}(\omega)$ in Eq. (17) with $\epsilon_{\mathrm{tox}}^{\infty}(\omega_{\mathrm{tox},L2}^2 - \omega^2)/(\omega_{\mathrm{tox},T2}^2 - \omega^2)$. From the solutions of the modified secular equation ($\omega_Q^{(-\mathrm{tox}1,1)}$, $\omega_Q^{(-\mathrm{tox}1,2)}$, $\omega_Q^{(-\mathrm{tox}1,3)}$, and $\omega_Q^{(-\mathrm{tox}1,4)}$) the relative top oxide TO1-phonon content of mode

i is

$$R^{(\mathrm{tox},1)}\big(\omega_Q^{(i)}\big) = \left|\frac{\Pi_{n=1}^{4}\big(\omega_Q^{(i)2} - \omega_Q^{(-\mathrm{tox}1,n)2}\big)}{\Pi_{j=1,i\neq j}^{5}\big(\omega_Q^{(i)2} - \omega_Q^{(j)2}\big)}\right|. \tag{36}$$

Like Eq. (34), the numerator and denominator are also quartic in ω^2. The relative top oxide TO2-phonon, bottom oxide TO1-phonon, and bottom oxide TO2-phonon contents ($R^{(\mathrm{tox},2)}$, $R^{(\mathrm{box},1)}$, and $R^{(\mathrm{box},2)}$) can be similarly defined. Hence the top oxide TO1-phonon content is

$$\Phi^{(\mathrm{tox},1)}\big(\omega_Q^{(i)}\big) = \frac{R^{(\mathrm{tox},1)}\big(\omega_Q^{(i)}\big)\big[1-\Phi^{(g)}\big(\omega_Q^{(i)}\big)\big]}{R^{(\mathrm{tox},1)}\big(\omega_Q^{(i)}\big) + R^{(\mathrm{tox},2)}\big(\omega_Q^{(i)}\big) + R^{(\mathrm{box},1)}\big(\omega_Q^{(i)}\big) + R^{(\mathrm{box},2)}\big(\omega_Q^{(i)}\big)}. \tag{37}$$

The top oxide TO2-phonon, bottom oxide TO1-phonon, and bottom oxide TO2-phonon contents ($\Phi^{(\mathrm{tox},2)}$, $\Phi^{(\mathrm{box},1)}$, and $\Phi^{(\mathrm{box},2)}$) can be similarly defined. Given Eqs. (34) and (37), the following sum rules have been numerically verified:

$$\sum_{i=1}^{5}\Phi^{(\mathrm{tox},1)}\big(\omega_Q^{(i)}\big) = \sum_{i=1}^{5}\Phi^{(\mathrm{tox},2)}\big(\omega_Q^{(i)}\big) = \sum_{i=1}^{5}\Phi^{(\mathrm{box},1)}\big(\omega_Q^{(i)}\big) = \sum_{i=1}^{5}\Phi^{(\mathrm{box},2)}\big(\omega_Q^{(i)}\big) = 1, \tag{38a}$$

$$\Phi^{(g)}\big(\omega_Q^{(i)}\big) + \Phi^{(\mathrm{tox},1)}\big(\omega_Q^{(i)}\big) + \Phi^{(\mathrm{tox},2)}\big(\omega_Q^{(i)}\big) + \Phi^{(\mathrm{box},1)}\big(\omega_Q^{(i)}\big) + \Phi^{(\mathrm{box},2)}\big(\omega_Q^{(i)}\big) = 1, \tag{38b}$$

for each mode $\omega_Q^{(i)}$.

F. Electron-IPP interaction

The *effective* scattering field of the top oxide TO1 phonon at frequency $\omega_Q^{(l)}$ can be obtained by combining Eqs. (29) and (37). We have

$$\phi_{Q,\omega}^{\mathrm{scr}}(d)\big|_{\omega=\omega_Q^{(l)}} = \left[\frac{\hbar\omega_Q^{(l)}}{2\Omega Q}\left(\frac{1}{\bar{\epsilon}_{\mathrm{tox}}^{\mathrm{HI},1}\big(\omega_Q^{(l)}\big) - \epsilon_{\mathrm{tox}}\big(\omega_Q^{(l)}\big)} - \frac{1}{\bar{\epsilon}_{\mathrm{tox}}^{\mathrm{LO},1}\big(\omega_Q^{(l)}\big) - \epsilon_{\mathrm{tox}}\big(\omega_Q^{(l)}\big)}\right)\Phi^{(\mathrm{tox},1)}\big(\omega_Q^{(l)}\big)\right]^{\frac{1}{2}}\mathcal{F}_{Q,\omega}^{(\mathrm{top})}\big|_{\omega=\omega_Q^{(l)}}. \tag{39}$$

This is only a part of the scattering field associated with mode $\omega_Q^{(l)}$. When we include the TO phonons of the top and bottom oxides, the total scattering field is

$$\begin{aligned}\phi_{Q,\omega}^{\mathrm{scr}}(d)\big|_{\omega=\omega_Q^{(l)}} = \left(\frac{\hbar\omega_Q^{(l)}}{2\Omega Q}\right)^{\frac{1}{2}}&\left[\sum_{\mu=1}^{2}\left(\frac{1}{\bar{\epsilon}_{\mathrm{tox}}^{\mathrm{HI},\mu}(\omega) - \epsilon_{\mathrm{tox}}(\omega)} - \frac{1}{\bar{\epsilon}_{\mathrm{tox}}^{\mathrm{LO},\mu}(\omega) - \epsilon_{\mathrm{tox}}(\omega)}\right)\Phi^{(\mathrm{tox},\mu)}(\omega)\big|\mathcal{F}_{Q,\omega}^{(\mathrm{top})}\big|^2\right.\\ &\left.+\sum_{\mu=1}^{2}\left(\frac{1}{\bar{\epsilon}_{\mathrm{box}}^{\mathrm{HI},\mu}(\omega) - \epsilon_{\mathrm{box}}(\omega)} - \frac{1}{\bar{\epsilon}_{\mathrm{box}}^{\mathrm{LO},\mu}(\omega) - \epsilon_{\mathrm{box}}(\omega)}\right)\Phi^{(\mathrm{box},\mu)}(\omega)\big|\mathcal{F}_{Q,\omega}^{(\mathrm{bot})}\big|^2\right]_{\omega=\omega_Q^{(l)}}^{\frac{1}{2}}.\end{aligned} \tag{40}$$

Generally, the graphene field operator can be written in the spinorial form as

$$\Psi(\mathbf{R},z) = \frac{1}{\sqrt{2\Omega}}\sum_{s=\pm1}\sum_{\mathbf{K}}\left[\begin{pmatrix}1\\ se^{i\theta_{\mathbf{K}}}\end{pmatrix}c_{\mathbf{K}}^{s\mathcal{K}} + \begin{pmatrix}e^{i\theta_{\mathbf{K}}}\\ s\end{pmatrix}c_{\mathbf{K}}^{s\mathcal{K}'}\right]e^{i\mathbf{K}\cdot\mathbf{R}}\sqrt{\delta(z-d)}, \tag{41}$$

where $\mathcal{K}$ ($\mathcal{K}'$) denotes the $\mathcal{K}$ ($\mathcal{K}'$) valley, and the $+$ ($-$) sign corresponds to the π (π^*) band; $c_{\mathbf{K}}^{s\mathcal{K}}$ ($c_{\mathbf{K}}^{s\mathcal{K}\dagger}$) is the annihilation (creation) operator of the s-band $\mathbf{K}$ electron state at the $\mathcal{K}$ valley. Therefore, the interaction term is

$$H_{\mathrm{int}} = \int dz\int d\mathbf{R}\,\Psi^{\dagger}(\mathbf{R},z)V(\mathbf{R},z)\Psi(\mathbf{R},z)$$

and, if we neglect the intervalley terms, simplifies to

$$H_{\mathrm{int}} \approx \sum_{l=1}^{3}\sum_{s_1,s_2}\sum_{\mathbf{K},\mathbf{Q}}M_Q^{(l)}\alpha_{s_1\mathbf{K}+\mathbf{Q},s_2\mathbf{K}}\big(c_{\mathbf{K}+\mathbf{Q}}^{s_1\mathcal{K}\dagger}c_{\mathbf{K}}^{s_2\mathcal{K}} + s_1s_2c_{\mathbf{K}+\mathbf{Q}}^{s_1\mathcal{K}'\dagger}c_{\mathbf{K}}^{s_2\mathcal{K}'}\big)\big(a_{\mathbf{Q}}^{(l)} + a_{-\mathbf{Q}}^{(l)\dagger}\big), \tag{42}$$

where $a_{\mathbf{Q}}^{(l)}$ ($a_{\mathbf{Q}}^{(l)\dagger}$) is the annihilation (creation) operator for the mode corresponding to $\mathbf{Q}$ and $\omega_Q^{(l)}$, and

$$\alpha_{s_1\mathbf{K}_1,s_2\mathbf{K}_2} = \frac{1+s_1s_2e^{-i(\theta_{\mathbf{K}_1}-\theta_{\mathbf{K}_2})}}{2}$$

is the overlap integral that comes from the inner product of the spinors; the electron-IPP coupling coefficient is

$$M_Q^{(l)} = \left(\frac{e^2\hbar\omega_Q^{(l)}}{2\Omega Q}\right)^{\frac{1}{2}} \left[\sum_{\mu=1}^{2}\left(\frac{1}{\bar{\epsilon}_{\text{tox}}^{\text{HI},\mu}(\omega)-\epsilon_{\text{tox}}(\omega)} - \frac{1}{\bar{\epsilon}_{\text{tox}}^{\text{LO},\mu}(\omega)-\epsilon_{\text{tox}}(\omega)}\right)\Phi^{(\text{tox},\mu)}(\omega)\left|\mathcal{F}_{Q,\omega}^{(\text{top})}\right|^2 + \sum_{\mu=1}^{2}\left(\frac{1}{\bar{\epsilon}_{\text{box}}^{\text{HI},\mu}(\omega)-\epsilon_{\text{box}}(\omega)} - \frac{1}{\bar{\epsilon}_{\text{box}}^{\text{LO},\mu}(\omega)-\epsilon_{\text{box}}(\omega)}\right)\Phi^{(\text{box},\mu)}(\omega)\left|\mathcal{F}_{Q,\omega}^{(\text{bot})}\right|^2\right]_{\omega=\omega_Q^{(l)}}^{\frac{1}{2}}. \tag{43}$$

G. Landau damping

At sufficiently short wavelengths, plasmons cease to be proper quasiparticle excitations because of Landau damping.[28] To model this phenomenon, albeit approximately, we take that to be the case when the pure graphene plasmon excitation, of which the dispersion $\omega = \omega_p(Q)$ is determined by the expression $1 - e^2G_Q(d,d)\Pi^{>}(Q,\omega) = 0$, enters the intraband single-particle excitation (SPE) continuum.[29] This happens when the plasmon branch crosses the electron dispersion curve, i.e., when $\omega_p = v_F Q$, and the wave vector at which this happens is Q_c. A common cutoff Q_c is used for all five IPP branches because we are constrained by the necessity to maintain the sum rule in Eq. (35). Thus, although the top IPP branch may undergo Landau damping from interband transitions, we assume that the IPP$_5$ branch modes are still well defined and do not undergo significant broadening. Selective omission of the top IPP branch while still retaining the lower four coupled plasmon-phonon branches would violate the sum rules in Eq. (38). If we set Q_c to be the point where the plasmonlike IPP$_5$ branch undergoes interband SPE Landau damping, then the lower branches would have to be replaced by SPP branches. This approximation is unreasonable because it assumes that the modes are broadened when they are not. On the other hand, it is less severe to assume that interband SPE Landau damping does not lead to significant broadening of the plasmonlike IPP modes. Admittedly, this is not a perfect way of handling the issue of Landau damping, and is a limitation of our theory, which assumes the spectral weight of the modes to be sharp δ function in frequency space.

When $Q < Q_c$, the electron-phonon coupling coefficient in Eq. (42) is that of Eq. (43). Although the lower-frequency IPP branches may undergo Landau damping from intraband SPE as $\omega_Q^{(l)} < v_F Q$, we still retain them because the sum rules in Eqs. (35) and (38) require us to maintain charge conservation.[28] On the other hand, when $Q > Q_c$, Landau damping is assumed to dominate all the IPP modes, and the coupling between the substrate SPP modes and the graphene plasmons can be ignored. Instead of scattering with five IPP modes for each given wave vector, we revert to using only four SPP modes. This allows us to satisfy the sum rules in Eq. (38). In this case, the electron-phonon coupling coefficient in Eq. (43) can be written as

$$M_Q^{(l)} = \left(\frac{e^2\hbar\omega_Q^{(l)}}{2\Omega Q}\right)^{\frac{1}{2}} \left[\sum_{\mu=1}^{2}\left(\frac{1}{\bar{\epsilon}_{\text{tox}}^{\text{HI},\mu}(\omega)-\epsilon_{\text{tox}}(\omega)} - \frac{1}{\bar{\epsilon}_{\text{tox}}^{\text{LO},\mu}(\omega)-\epsilon_{\text{tox}}(\omega)}\right)\Phi^{(\text{tox},\mu)}(\omega)\left|\mathcal{F}_{Q,\omega}^{(\text{top})}\right|^2 + \sum_{\mu=1}^{2}\left(\frac{1}{\bar{\epsilon}_{\text{box}}^{\text{HI},\mu}(\omega)-\epsilon_{\text{box}}(\omega)} - \frac{1}{\bar{\epsilon}_{\text{box}}^{\text{LO},\mu}(\omega)-\epsilon_{\text{box}}(\omega)}\right)\Phi^{(\text{box},\mu)}(\omega)\left|\mathcal{F}_{Q,\omega}^{(\text{bot})}\right|^2\right]_{\omega=\omega_Q^{(l)}}^{\frac{1}{2}}, \tag{44}$$

where $l = \text{SPP}_1$ to SPP_4 indexes the four SPP branches. Although Eq. (44) looks identical to Eq. (43), the individual terms in the former expression are different. For instance, the plasmonless secular equation in Eq. (33) is used to determine $\omega_Q^{(\text{SPP1})}$, $\omega_Q^{(\text{SPP2})}$, $\omega_Q^{(\text{SPP3})}$, and $\omega_Q^{(\text{SPP4})}$. The phonon content in Eq. (44) is defined slightly differently. For example, because $\Phi^{(g)}(\omega) = 0$, we write $\Phi^{(\text{tox},1)}(\omega)$ as

$$\Phi^{(\text{tox},1)}(\omega) = \frac{R^{(\text{tox},1)}(\omega)}{R^{(\text{tox},1)}(\omega) + R^{(\text{tox},2)}(\omega) + R^{(\text{box},1)}(\omega) + R^{(\text{box},2)}(\omega)}, \tag{45}$$

where

$$R^{(\text{tox},1)}\big(\omega_Q^{(i)}\big) = \left|\frac{\Pi_{n=1}^{3}\big(\omega_Q^{(i)2} - \omega_Q^{(-\text{tox}1,n)2}\big)}{\Pi_{j=1,i\neq j}^{4}\big(\omega_Q^{(i)2} - \omega_Q^{(j)2}\big)}\right|. \tag{46}$$

The frequencies $\omega_Q^{(-\text{tox}1,1)}$, $\omega_Q^{(-\text{tox}1,2)}$, and $\omega_Q^{(-\text{tox}1,3)}$ are frequencies calculated with Eq. (33) but with $\epsilon_{\text{tox}}(\omega)$ replaced with $\epsilon_{\text{tox}}^{\infty}(\omega_{\text{tox},L2}^2 - \omega^2)/(\omega_{\text{tox},T2}^2 - \omega^2)$. Unlike Eq. (36), the denominator and numerator in Eq. (46) are cubic in

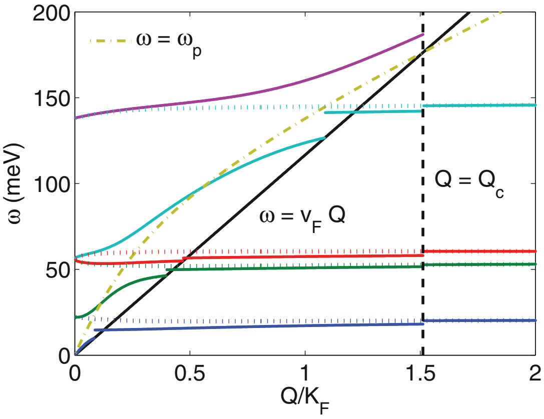

FIG. 2. (Color online) Dispersion relation of coupled interfacial plasmon-phonon system with $n = 10^{12}$ cm^{-2} for a substrate of SiO$_2$ and 20 nm of HfO$_2$ top dielectric. The five IPP branches are drawn in thick lines, while the SPP branches are shown in dotted lines. The graphene plasmon dispersion (ω_p) is plotted with a dot-dashed line. The cutoff $Q = Q_c$ is determined from the crossing of $\omega = v_F Q$ and the plasma branch $\omega_p(Q)$. In the limits $Q \rightarrow 0$ and $Q \rightarrow \infty$, the IPP branches converge to the pure phonon and plasmon branches. In between, they are a mix of the pure branches.

ω^2. $\Phi^{(\mathrm{tox},2)}(\omega)$, $\Phi^{(\mathrm{box},1)}(\omega)$, and $\Phi^{(\mathrm{box},2)}(\omega)$ are similarly defined.

III. NUMERICAL METHODOLOGY

Having set up the theoretical framework for the electron-IPP interaction, we discuss in this section the details of the calculation of the dispersion of the coupled interfacial plasmon-phonon modes, the electron-IPP coupling coefficient, the momentum relaxation rate, and the remote-phonon-limited electron mobility.

A. Interfacial plasmon-phonon dispersion

In this section, we compute the dispersion relation ($\omega_Q^{(l)}$) by solving Eq. (17). For *simplicity*, we use the zero-temperature, *long-wavelength* approximation for $\Pi(Q,\omega)$ in the random phase approximation:[29,30]

$$\Pi(Q,\omega) = \Theta(\omega - v_F Q)\Pi^{>}(Q,\omega) + \Theta(v_F Q - \omega)\Pi^{<}(Q,\omega), \tag{47}$$

where

$$\Pi^{>}(Q,\omega) = \frac{Q^2 v_F (\pi n)^{\frac{1}{2}}}{\pi\hbar\omega^2}, \quad \Pi^{<}(Q,\omega) = -\frac{2(\pi n)^{\frac{1}{2}}}{\pi\hbar v_F},$$

and n is the electron density.

TABLE I. Parameters [see Eq. (1)] used in computing the dispersion relation and scattering rates. They are taken from Refs. 26 and 19.

	SiO$_2$	HfO$_2$
$\epsilon_{\mathrm{ox}}^{0}$ (ϵ_0)	3.90	22.00
$\epsilon_{\mathrm{ox}}^{i}$ (ϵ_0)	3.05	6.58
$\epsilon_{\mathrm{ox}}^{\infty}$ (ϵ_0)	2.50	5.03
ω_{TO1} (meV)	55.60	12.40
ω_{TO2} (meV)	138.10	48.35
d (nm)	0.35	

In Fig. 2, we show the dispersion relation for an SiO$_2$ substrate with a 20 nm HfO$_2$ top dielectric at $n = 10^{12}$ cm^{-2}, with the parameters taken from Table I. The five coupled IPP branches are drawn with solid lines, while the four SPP branches are plotted in dotted lines. The SPP branches are determined from Eq. (33), while the plasmon branch (ω_p) is determined from the zeros of the equation,

$$1 - G_Q(d,d)e^2\Pi^{>}(Q,\omega), \tag{48}$$

which gives the dispersion of the *pure* graphene plasmons when the frequency dependence of the substrate dielectric function is neglected and only the effect of the image charges is taken into account.

Given the discontinuity of $\Pi(Q,\omega)$ in the long wavelength approximation, the dispersion of the IPP branches is also discontinuous, and this can be seen in Fig. 2. To work around this, we first calculate the IPP branches ($\omega_Q^{>}$) using Eqs. (17) but with $\Pi(Q,\omega) = \Pi^{>}(Q,\omega)$. We also calculate the IPP branches ($\omega_Q^{<}$) with $\Pi(Q,\omega) = \Pi^{<}(Q,\omega)$. The absence of any ω dependence in $\Pi^{<}(Q,\omega)$ means that there are only four $\omega_Q^{<}$ solutions for each $\mathbf{Q}$. The final solution is obtained by setting

$$\omega(Q) = \Theta(\omega_Q^{>} - v_F Q)\omega_Q^{>} + \Theta(v_F Q - \omega_Q^{>})\omega_Q^{<},$$

where $\Theta(\cdots)$ is the Heaviside function. In other words, we "stitch" the four lowest $\omega_Q^{>}$ and $\omega_Q^{<}$ solutions together. This method allows us to define an IPP branch that is defined for all values of Q. We also introduce a Landau damping cutoff $Q = Q_c$, which is the root of the equation $\omega_p(Q) = v_F Q$. Beyond the Landau damping cutoff, $Q > Q_c$, the four SPP solutions are used instead.

In Fig. 2, we observe that in the long and short wavelength limits ($Q \rightarrow 0$ and $Q \rightarrow \infty$), the IPP branches converge asymptotically to the "pure" plasmon and SPP branches, i.e.,

$$\lim_{Q\rightarrow 0} \begin{pmatrix} \omega_Q^{(\mathrm{IPP1})} \\ \omega_Q^{(\mathrm{IPP2})} \\ \vdots \\ \omega_Q^{(\mathrm{IPP5})} \end{pmatrix} = \begin{pmatrix} \omega_p \\ \omega_Q^{(\mathrm{SPP1})} \\ \vdots \\ \omega_Q^{(\mathrm{SPP4})} \end{pmatrix}$$

and

$$\lim_{Q\rightarrow\infty} \begin{pmatrix} \omega_Q^{(\mathrm{IPP1})} \\ \vdots \\ \omega_Q^{(\mathrm{IPP4})} \\ \omega_Q^{(\mathrm{IPP5})} \end{pmatrix} = \begin{pmatrix} \omega_Q^{(\mathrm{SPP1})} \\ \vdots \\ \omega_Q^{(\mathrm{SPP4})} \\ \omega_p \end{pmatrix}.$$

At intermediate values of Q, the IPP branches are a mixture of the pure branches.

B. Electron-phonon coupling

Here, the electron-phonon coupling coefficients $M_Q^{(l)}$ of the IPP and the SPP modes corresponding to the phonon dispersion in Fig. 2 are compared. Recall that the IPP modes are formed through the hybridization of the SPP and graphene plasmon modes, and their coupling to the graphene electrons are different to that of the SPP modes. We plot $M_Q^{(l)}(\Omega/A)^{1/2}$, where A is the area of the primitive unit cell in SLG, for the SPP and IPP modes in Fig. 3(a). At longer wavelengths in the limit $Q \to 0$ [Fig. 3(b)], the strength of the antiscreening diminishes, and the electron-IPP coupling coefficients converge to those of the electron-SPP coupling coefficients, i.e.,

$$\lim_{Q\to 0}\begin{pmatrix} M_Q^{(\mathrm{IPP2})} \\ \vdots \\ M_Q^{(\mathrm{IPP5})} \end{pmatrix} = \begin{pmatrix} M_Q^{(\mathrm{SPP1})} \\ \vdots \\ M_Q^{(\mathrm{SPP4})} \end{pmatrix},$$

because $\lim_{Q\to 0}\Pi(Q,\omega) = 0$ and the effects of screening diminish at small Q. This is expected because the corresponding excitation frequencies also converge, i.e.,

$$\lim_{Q\to 0}\begin{pmatrix} \omega_Q^{(\mathrm{IPP2})} \\ \vdots \\ \omega_Q^{(\mathrm{IPP5})} \end{pmatrix} = \begin{pmatrix} \omega_Q^{(\mathrm{SPP1})} \\ \vdots \\ \omega_Q^{(\mathrm{SPP4})} \end{pmatrix}.$$

This can be seen in Fig. 2.

We observe in Fig. 2 discontinuities in the IPP dispersion, which in turn lead to discontinuities in the electron-IPP coupling coefficient $M_Q^{(l)}$ (Fig. 3) as we will see later. The appearance of these discontinuities follow from the discontinuous $\Pi(Q,\omega)$ in Eq. (47). In Fig. 2, IPP excitations in the region $\omega < v_F Q$ correspond to intraband transitions between electron states in the linear dispersion approximation. Conversely, excitations in the region $\omega > v_F Q$ correspond to interband transitions. When $\omega < v_F Q$, $\Pi(Q,\omega) = \Pi^{<}(Q,\omega)$ in Eq. (47) has no ω dependence, giving us a static screening; when $\omega > v_F Q$, the ω dependence of $\Pi(Q,\omega) = \Pi^{>}(Q,\omega)$ gives us dynamic screening. This means that the effects of dynamic screening are more important at low electron densities where interband transitions are more probable.

C. Scattering rate and remote phonon-limited mobility formulas

The momentum relaxation rate for an electron in band s with wave vector $\mathbf{K}$ can be written as

$$\Gamma_{\mathrm{RP}}(s,\mathbf{K}) = \frac{2\pi}{\hbar}\sum_{l}\sum_{s'}\sum_{\mathbf{Q}}\left|M_Q^{(l)}\alpha_{s\mathbf{K}+\mathbf{Q},s'\mathbf{K}}\right|^2[1 - ss'\cos(\theta_{\mathbf{K}+\mathbf{Q}} - \theta_{\mathbf{K}})]\left\{\left[1 + N_B\left(\omega_Q^{(l)}\right)\right]\left[1 - f(E_{s'\mathbf{K}+\mathbf{Q}})\right]\right.$$
$$\left.\times\,\delta\left(E_{s\mathbf{K}} - E_{s'\mathbf{K}+\mathbf{Q}} - \hbar\omega_Q^{(l)}\right) + N_B\left(\omega_Q^{(l)}\right)\left[1 - f(E_{s'\mathbf{K}+\mathbf{Q}})\right]\delta\left(E_{s\mathbf{K}} - E_{s'\mathbf{K}+\mathbf{Q}} + \hbar\omega_Q^{(l)}\right)\right\}, \qquad (49)$$

where $N_B(\omega) = (e^{\hbar\omega/k_BT} - 1)^{-1}$, $f(E) = [e^{(E-E_F)/k_BT} + 1]^{-1}$, and $E_{s\mathbf{K}} = s\hbar v_F|\mathbf{K}|$. In assuming the latter expression, we use the Dirac-conical approximation. Equation (49) automatically includes the Fermi-Dirac distribution and Pauli blocking of the final states, and remains applicable when the doping level is high.

The expression for the IPP/SPP-limited part of the electrical conductivity is

$$\sigma_{\mathrm{RP}} = \frac{g_s g_v e^2}{4\pi\hbar^2 k_B T}\int_0^\infty f(E - E_F)$$
$$\times\,[1 - f(E - E_F)]\Gamma_{tr}(E)^{-1}E\,dE, \qquad (50)$$

where $g_s = 2$ and $g_v = 2$ are the spin and valley degeneracies, respectively. Only the contribution from the conduction band is included in Eq. (50). We use Eqs. (49) and (50) to compute the IPP- or SPP-limited electrical conductivity by setting

$$\Gamma_{\mathrm{tr}}(E) = \Gamma_{\mathrm{RP}}(s,\mathbf{K}). \qquad (51)$$

In making this approximation, we ignore the other effects (ripples, charged impurity, acoustic phonons, optical phonons, etc). The scattering rates from the acoustic and optical phonons tend to be significantly smaller and are not the limiting factor in electrical transport in supported graphene.[31] Impurity scattering tends to be the dominant limiting factor, but its effects can be reduced by varying fabrication conditions. Thus the conductivity using Eq. (51) gives us its upper bound. We calculate the remote phonon-limited mobility as

$$\mu_{\mathrm{RP}} = \frac{\sigma_{\mathrm{RP}}}{en}, \qquad (52)$$

where $n = \frac{g_s g_v}{2\pi\hbar^2 v_F^2}\int_0^\infty f(E - E_F)E\,dE$ is the electron density. We compute the remote phonon-limited mobility numerically, using the well-known Gilat-Raubenheimer method[32] to discretize the sum in Eq. (49).

IV. EFFECT OF TOP-GATE THICKNESS ON ELECTRON MOBILITY

In this section, we look at the effects of the top oxide thickness on the electron-IPP and electron-SPP coupling. The latter case corresponds to the case without plasmonic coupling and serves as a basis of comparison when we consider electron-IPP interaction. We use the computed electron-remote phonon coupling to determine the top oxide thickness dependence of μ_{IPP}.

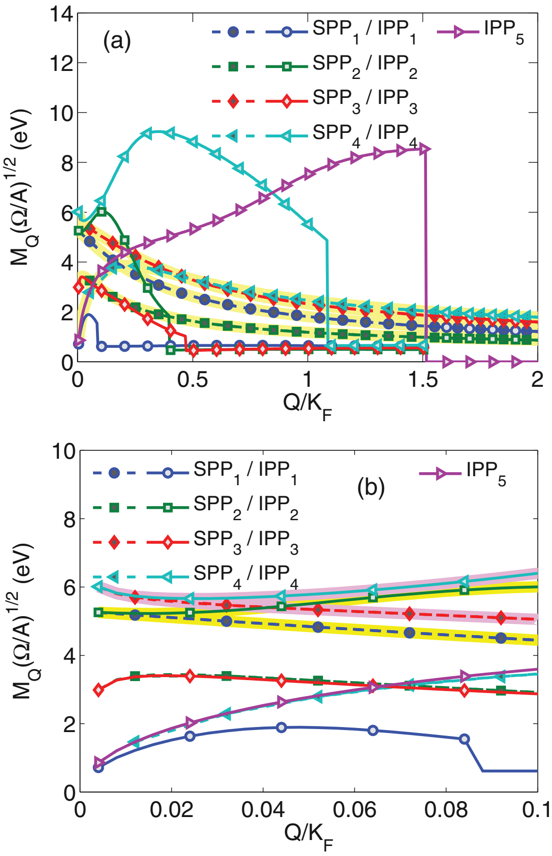

FIG. 3. (Color online) (a) Plot of $M_Q^{(l)}(\Omega/A)^{1/2}$ for $n = 10^{12}$ cm^{-2} in SiO$_2$-supported graphene with 20 nm HfO$_2$ top dielectric. (b) The same plot but at small Q. $M_Q^{(\text{SPP1})}$ (solid square) and $M_Q^{(\text{IPP2})}$ (open diamond) are highlighted. As $Q \rightarrow 0$, the two converge. Similarly, $M_Q^{(\text{SPP3})}$ (solid circle) and $M_Q^{(\text{IPP4})}$ (open triangle) converge as $Q \rightarrow 0$.

A. Without plasmonic coupling

We first look at the case where the coupling with graphene plasmons is neglected. This allows us to isolate the effects of the top oxide thickness and the coupling between the dipoles in the top and bottom oxides. In a SLG sheet with no HfO$_2$ top dielectric and a semi-infinite SiO$_2$ substrate, the excitation energies of the substrate are determined by Eq. (19), i.e., $\epsilon_{\text{box}}(\omega) + \epsilon_0 = 0$, which follows from the continuity of the electric field and displacement across the substrate-air interface, and are independent of the wave vector Q ($\omega^{(\text{SiO}_2,1)} = 61$ meV and $\omega^{(\text{SiO}_2,2)} = 149$ meV). Likewise, for a SLG sheet supported on a semi-infinite HfO$_2$ substrate, the excitation energies computed from the equation $\epsilon_{\text{tox}}(\omega) + \epsilon_0 = 0$ are also Q independent ($\omega^{(\text{HfO}_2,1)} = 21.3$ meV and $\omega^{(\text{HfO}_2,2)} = 55.1$ meV). However, in SLG supported on a semi-infinite SiO$_2$ substrate with a HfO$_2$ top dielectric of finite thickness (t_{ox}), the dipole excitations in the HfO$_2$ top dielectric and the SiO$_2$ substrate are coupled, altering the dispersion of the SPP excitations. We compute the SPP dispersion using Eq. (33) for $t_{\text{ox}} = 2$ and 200 nm, and plot them in Fig. 4. Figure 4(a) shows the SPP dispersion for $t_{\text{ox}} = 2$ nm. The SPP energy is Q dependent for all four branches. The coupled SPP branches diverge from the uncoupled SPP branches as $Q \rightarrow 0$. On the other hand, in the short wavelength limit, they converge towards the uncoupled SPP energies, i.e.,

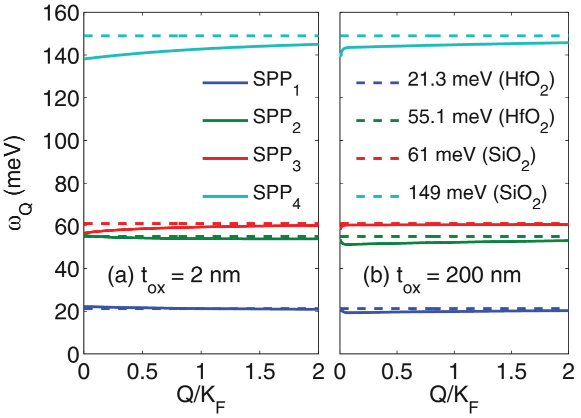

FIG. 4. (Color online) Surface polar phonon dispersion in SiO$_2$-supported SLG with (a) 2 nm of and (b) 200 nm of HfO$_2$ top dielectric at $n = 10^{12}$ cm^{-2}. The SPP modes ($\omega_Q^{(\text{SPP1})}$, $\omega_Q^{(\text{SPP2})}$, $\omega_Q^{(\text{SPP3})}$, and $\omega_Q^{(\text{SPP4})}$) are drawn with solid lines. The dispersion of SiO$_2$-supported and HfO$_2$-supported SLG with no top dielectric are plotted in dashed lines. K_F is the Fermi wave vector.

$$\lim_{Q\rightarrow\infty}\begin{pmatrix}\omega_Q^{(\text{SPP1})}\\ \omega_Q^{(\text{SPP2})}\\ \omega_Q^{(\text{SPP3})}\\ \omega_Q^{(\text{SPP4})}\end{pmatrix} = \begin{pmatrix}\omega^{(\text{HfO}_2,1)}\\ \omega^{(\text{HfO}_2,2)}\\ \omega^{(\text{SiO}_2,1)}\\ \omega^{(\text{SiO}_2,2)}\end{pmatrix},$$

as expected. In either limit, the excitation energy of the coupled SPP modes are close to that of the uncoupled SPP modes. This suggests that even with an ultrathin top oxide, the SPP dispersion does not change significantly.

Although the dispersion of the coupled SPP modes is similar to that of the uncoupled SPP modes, the same cannot be said of the electron-SPP coupling. We plot the electron-SPP coupling coefficients in Fig. 5 for (a) $t_{\text{ox}} = 200$ nm, (b) 20 nm, and (c) 2 nm at $n = 10^{12}$ cm^{-2}. In Fig. 5(a), the coupling coefficients M_Q in top-gated and bottom-gated SLG scale as $Q^{-1/2}$ in the long wavelength limit ($Q \rightarrow 0$). The electron-SPP coupling in top-gated SLG is smaller than that in bottom-gated SLG because of mutual screening by the top and bottom oxides in top-gated SLG. When $t_{\text{ox}} = 20$ nm, the long wavelength limit of M_Q does not scale as $Q^{-1/2}$. This is because the top oxide thickness provides a natural wave vector cutoff. When $t_{\text{ox}} = 20$ nm, $Q = t_{\text{ox}}^{-1}$ is around $0.28K_F$, given that the Fermi wave vector is $K_F = \sqrt{\pi n}$. In Fig. 5(b), we observe that M_Q starts to deviate significantly from the $Q^{-1/2}$ behavior at around $Q = t_{\text{ox}}^{-1}$. With ultrathin top oxide ($t_{\text{ox}} = 2$ nm), the cutoff ($t_{\text{ox}}^{-1} = 2.8K_F$) is even larger. Therefore, in Fig. 5(c), the coupling coefficient deviates from the $Q^{-1/2}$ behavior over the entire range of Q values. From the plots in Fig. 5, we see that the electron-SPP coupling becomes weaker with decreasing t_{ox}. At small t_{ox}, the metal layer is closer to the bottom and top oxide-air interfaces, and screens more effectively the scattering charge distribution.

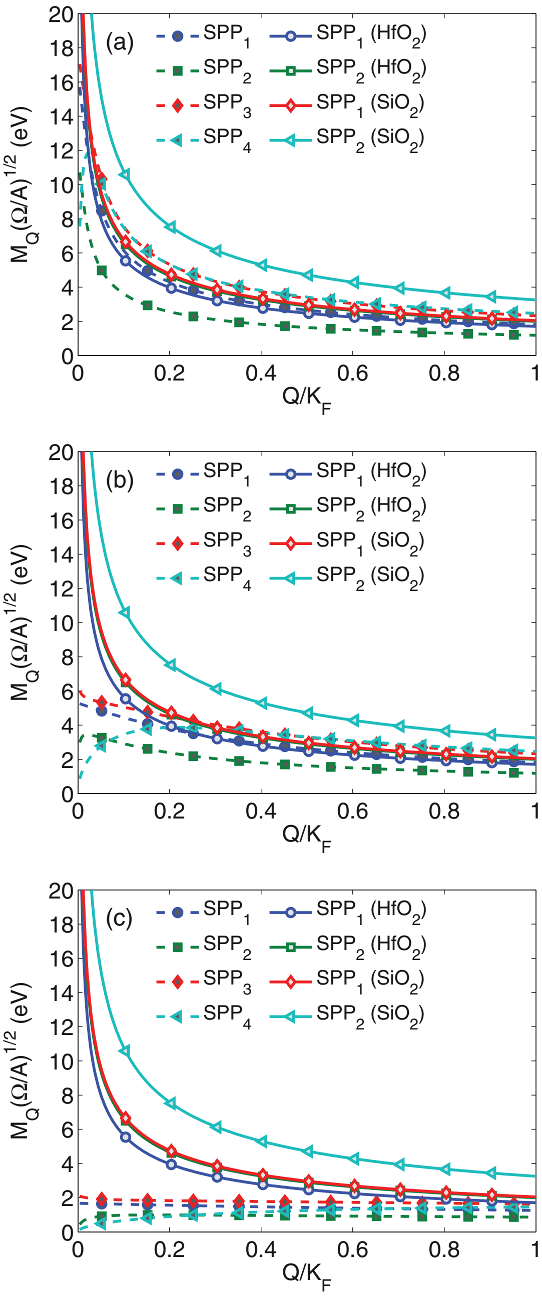

FIG. 5. (Color online) Electron-SPP coupling coefficients in SiO$_2$-supported SLG with (a) 200 nm, (b) 20 nm, and (c) 2 nm of HfO$_2$ top dielectric at $n = 10^{12}$ cm^{-2}. The uncoupled electron-SPP coupling coefficients ($M_Q^{(\mathrm{SPP1})}$, $M_Q^{(\mathrm{SPP2})}$, $M_Q^{(\mathrm{SPP3})}$, and $M_Q^{(\mathrm{SPP4})}$) are drawn with dashed lines and solid symbols. The dispersion of SiO$_2$-supported and HfO$_2$-supported SLG with no top dielectric are plotted in solid lines and open symbols. K_F is the Fermi wave vector.

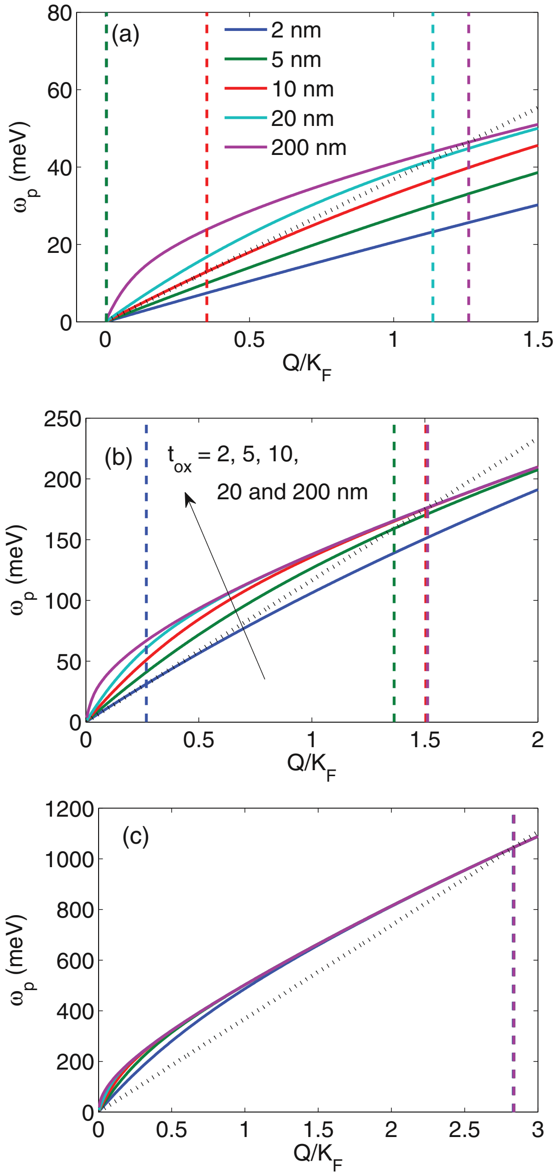

FIG. 6. (Color online) Plasmon dispersion at (a) $n = 10^{11}$ cm^{-2}, (b) 10^{12} cm^{-2}, and (c) 10^{13} cm^{-2} for $t_{\mathrm{ox}} = 2$, 5, 10, 20, and 200 nm plotted in solid lines. In each subfigure, the lowest (highest) branch corresponds to $t_{\mathrm{ox}} = 2$ nm ($t_{\mathrm{ox}} = 2$ nm). The electron energy dispersion is drawn with dotted lines. The dashed lines show the Landau cutoff (Q_c) at the intersection of the different plasmon dispersion curves and the electron energy dispersion. The leftmost (rightmost) line corresponds to $t_{\mathrm{ox}} = 2$ nm ($t_{\mathrm{ox}} = 200$ nm).

B. With plasmonic coupling

Next, we take plasmonic coupling to the SPP modes into account. In order to understand the effects of plasmonic coupling, we first look at the energy dispersion $\omega_p(Q)$ of the plasmons. It is important because Landau damping sets in when $Q > Q_c$, where Q_c is the cutoff wave vector and determined by the equation $Q_c = \omega_p(Q_c)/v_F$. Where there is Landau damping, the plasmons are no longer good quasiparticle excitations and cannot couple to the SPP modes. Thus, at such large wave vectors, plasmonic coupling and screening cannot take place.

In SLG, the plasmon dispersion is determined by Eq. (48). Physically, the energy of the plasmon modes depends on the electron-electron interaction strength, which is proportional to the $G_Q(d,d)$ term in Eq. (48). Hence, when the interaction strength is weaker, the energy of the plasmon excitation also decreases. Figure 6 shows the plasmon dispersion computed for different t_{ox} at various electron densities (a) $n = 10^{11}$ cm^{-2}, (b) 10^{12} cm^{-2}, and (c) 10^{13} cm^{-2}. In Fig. 6(a), the plasmon dispersion curves at $n = 10^{11}$ cm^{-2} are plotted. As

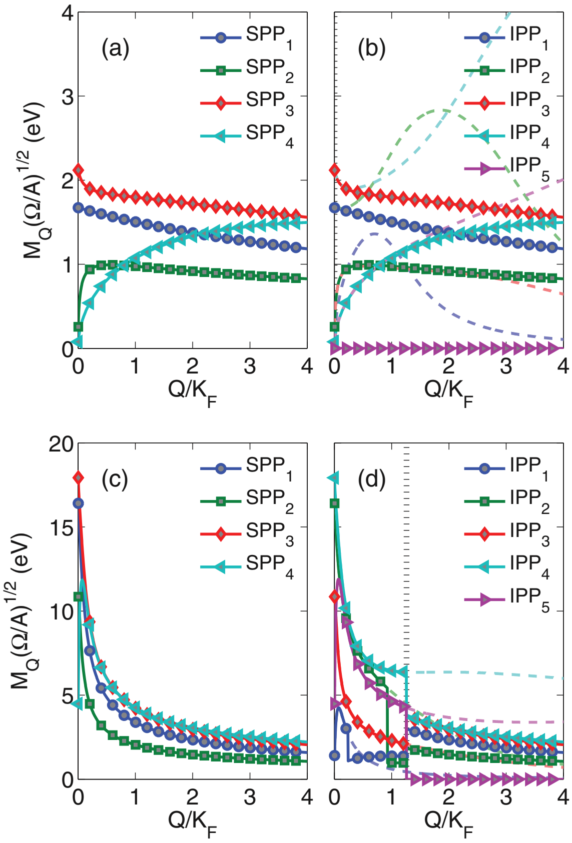

FIG. 7. (Color online) Plot of (a) electron-SPP and (b) electron-IPP coupling coefficients at $n = 10^{11}$ cm^{-2} for $t_{\mathrm{ox}} = 2$ nm. The corresponding electron-SPP and electron-IPP coupling coefficients plots for $t_{\mathrm{ox}} = 200$ nm are shown in (c) and (d), respectively. The coupling coefficients without Landau damping are plotted in dashed lines in (b) and (d). The dotted line in (b) and (d) indicates the position of the cutoff wave vector Q_c.

t_{ox} decreases, $\omega_p(Q)$ also decreases because a thinner top oxide increases the image charge screening effect of the metal layer and thus weakens electron-electron interaction in the SLG. The energy dispersion of the SLG electron is also shown. Given that Q_c is determined by the intersection of ω_p and $v_F Q$ (plotted in dotted lines in Fig. 6), we find that Q_c shifts further to the right as t_{ox} increases. In other words, plasmonic coupling and screening become weaker as the top oxide becomes thinner. Figure 6(a) shows that the Q_c for $t_{\mathrm{ox}} = 2$ and 5 nm is essentially zero when $n = 10^{11}$ cm^{-2}. In other words, there is no plasmonic coupling. At larger t_{ox} values, Q_c moves away from the origin. Figure 6(b) shows the plasmon dispersion for $n = 10^{12}$ cm^{-2}. The larger electron density also implies a higher ω_p and larger Q_c. Except for $t_{\mathrm{ox}} = 2$ nm, the plasmonic coupling and screening for other t_{ox} are also significant. In Fig. 6(c), the large electron density ($n = 10^{13}$ cm^{-2}) results in essentially the same Q_c for all t_{ox} values because the plasmon dispersion curves converge at large Q.

Given the difference in the plasmon dispersion and the concomitant onset of Landau damping, we look next at how the difference in t_{ox} and plasmonic coupling affects electron-IPP coupling. Figure 7 shows the electron-SPP and electron-IPP coupling coefficients at $n = 10^{11}$ cm^{-2} for $t_{\mathrm{ox}} = 2$ and 200 nm. For $t_{\mathrm{ox}} = 2$ nm, the electron-SPP [Fig. 7(a)] and electron-IPP [Fig. 7(b)] coupling coefficients are essentially the same, because Q_c is set at the origin. Hence all the IPP modes do not couple to the plasmons and are heavily damped. The electron-IPP coupling coefficients without Landau damping are also drawn in dashed lines in Fig. 7(b) for comparison.

At $t_{\mathrm{ox}} = 200$ nm, the screening effect of the metal layer becomes much weaker. Hence the electron-SPP [Fig. 7(c)] and electron-IPP [Fig. 7(d)] coupling coefficients are different at long wavelengths, because Q_c is not at the origin. Nonetheless, when $Q < Q_c$, the undamped electron-IPP coupling coefficients are similar to the electron-SPP coupling coefficients because of the weak plasmonic coupling. For example, we notice that $M_Q^{(\mathrm{IPP5})}$ [right-pointing triangles in Fig. 7(d)] is close to $M_Q^{(\mathrm{SPP4})}$ [left-pointing triangles in Fig. 7(c)].

At $n = 10^{12}$ cm^{-2}, the effects of the top oxide thickness are different. The higher electron density implies higher plasmon energies and, thus, a rightward shift in Q_c and the onset of Landau damping. The undamped IPP modes are also more

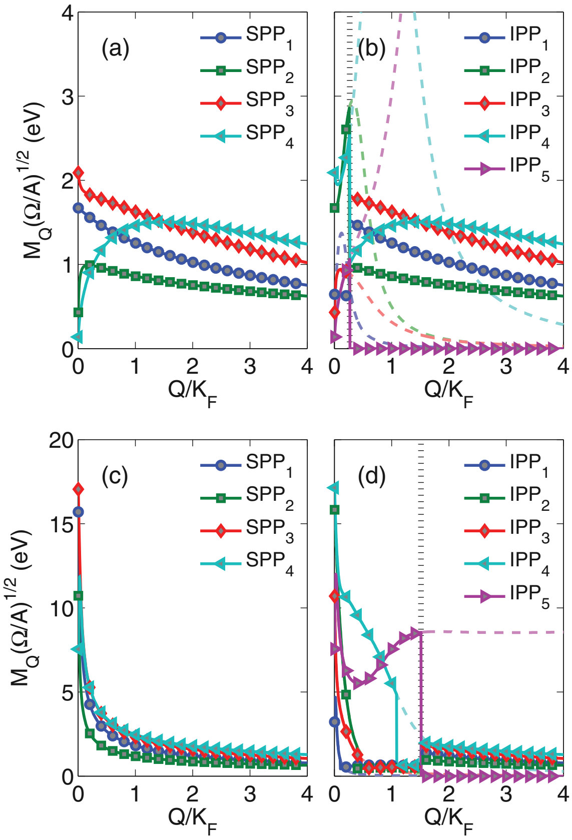

FIG. 8. (Color online) Plot of (a) electron-SPP and (b) electron-IPP coupling coefficients at $n = 10^{12}$ cm^{-2} for $t_{\mathrm{ox}} = 2$ nm. Only a small fraction of the IPP modes are not Landau damped. The corresponding electron-SPP and electron-IPP coupling coefficients plots for $t_{\mathrm{ox}} = 200$ nm are shown in (c) and (d), respectively. The coupling coefficients without Landau damping are plotted in dashed lines in (b) and (d). The dotted line in (b) and (d) indicates the position of the cutoff wave vector Q_c. In (d), a large fraction of the IPP modes are coupled to the plasmons because the onset of Landau is significantly delayed.

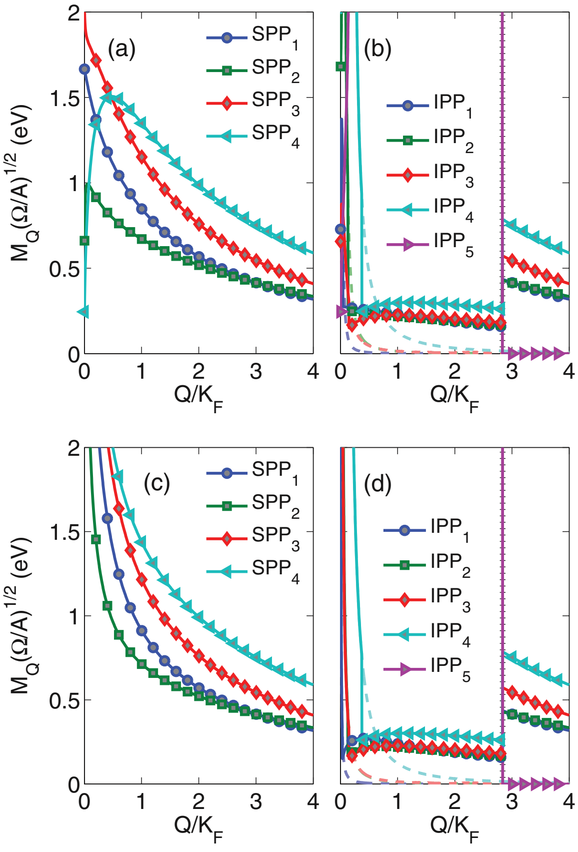

FIG. 9. (Color online) Plot of (a) electron-SPP and (b) electron-IPP coupling coefficients at $n = 10^{13}$ cm^{-2} for $t_{\text{ox}} = 2$ nm. The corresponding electron-SPP and electron-IPP coupling coefficients plots for $t_{\text{ox}} = 200$ nm are shown in (c) and (d), respectively. The coupling coefficients without Landau damping are plotted in dashed lines in (b) and (d). The dotted line in (b) and (d) indicates the position of the cutoff wave vector Q_c.

strongly coupled to the plasmons. Figures 8(a) and 8(b) show the electron-SPP and electron-IPP coupling coefficients at $n = 10^{12}$ cm^{-2} for $t_{\text{ox}} = 2$ nm. Unlike Fig. 7(b), Q_c is no longer at the origin. Thus a small but significant fraction of the IPP modes are not Landau damped, as we can see in Fig. 8(b). For $t_{\text{ox}} = 200$ nm, the electron-SPP and electron-IPP coefficients are plotted in Figs. 8(c) and 8(d). Landau damping is shifted to the right of $Q = K_F$ because of the much thicker top oxide. Hence a significant fraction of the IPP modes are coupled to the plasmons and are not Landau damped.

At $n = 10^{13}$ cm^{-2}, the effects of the top oxide thickness on electron-IPP coupling are similar. In Fig. 6(c), we see that Q_c is essentially the same for all t_{ox} values, i.e., $Q_c \sim 3K_F$. This implies that the effect of Landau damping is negligible for electron-IPP coupling. Figures 9(a) and 9(b) show the electron-SPP and electron-IPP coupling coefficients at $n = 10^{13}$ cm^{-2} for $t_{\text{ox}} = 2$ nm, while Figs. 9(c) and 9(d) show the electron-SPP and electron-IPP coupling coefficients for $t_{\text{ox}} = 200$ nm. Although the electron-SPP coupling coefficients for $t_{\text{ox}} = 2$ nm [Fig. 9(a)] and $t_{\text{ox}} = 200$ nm [Fig. 9(c)] are very different, the electron-IPP coefficients in Figs. 9(b) and 9(d) are very similar because of the strong plasmonic coupling.

C. Mobility dependence on top oxide thickness

We use Eq. (52) to compute the SPP/IPP-limited mobility for different t_{ox} at different electron densities ($n = 10^{11}$, 10^{12}, and 10^{13} cm^{-2}). Figure 10 shows the remote phonon-limited mobility. In Fig. 10(a), we ignore plasmonic coupling and the electron-SPP coupling coefficients are used to compute the mobility μ_{SPP}. In Fig. 10(b), the mobility from electron-IPP scattering μ_{IPP} is calculated instead. Without plasmonic coupling, μ_{SPP} decreases with increasing electron density and top oxide thickness because a thicker t_{ox} reduces the screening effect of the metal gate on electron-SPP coupling. The increase of μ_{SPP} with decreasing t_{ox} also becomes smaller at larger n because a smaller proportion of electron-SPP scattering events are affected by the heavily screened long wavelength SPP modes. These two results parallel those found for charged impurity scattering in top-gated SLG[8]: a thinner top oxide improves the mobility as a result of screening by the metal gate but this mobility improvement is smaller at higher electron densities. A similar gate screening effect was reported by Laikhtman and Solomon,[33] who found that a thinner HfO$_2$ leads to an increase in remote-phonon-limited channel mobility in Si.

Figure 10(b) shows the plot of μ_{IPP} versus t_{ox}. At $n = 10^{11}$ cm^{-2}, plasmonic coupling and dynamic screening is weak. The Landau damping is also substantial. Thus the dependence of μ_{IPP} on t_{ox} is similar to the dependence of μ_{SPP}. For $t_{\text{ox}} = 200$ nm, we have $\mu_{\text{IPP}} \approx 1500$ cm^{2}V^{-1}s^{-1}. At $n = 10^{12}$ cm^{-2} and $t_{\text{ox}} = 2$ nm, μ_{SPP} and μ_{IPP} are the same because of the lack of plasmonic screening. However, as t_{ox} increases, μ_{IPP} also increases because the plasmons are screened less and plasmonic coupling is larger. This highlights two screening phenomena by the top metal gate. First, the top metal gate directly screens the interaction between the electrons and the SPP modes in the oxides. Secondly, it also screens the plasmons which screen the interaction between electrons and the SPP modes. This screening of, not by, the plasmons results in a stronger interaction between the electrons and the SPP modes. Therefore, at low electron densities, the decrease in μ_{IPP} with a thicker t_{ox} at $n = 10^{11}$ cm^{-2} can be explained by the dominance of the first screening phenomenon. On the other hand, the increase in μ_{IPP} with t_{ox} at $n = 10^{12}$ cm^{-2} is a consequence of the dominance of the latter

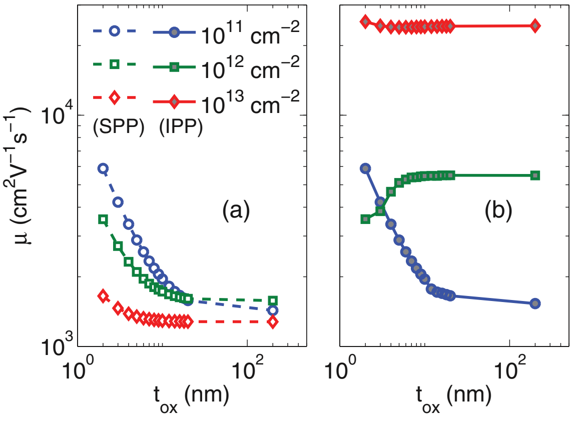

FIG. 10. (Color online) Plot of (a) μ_{SPP} and (b) μ_{IPP} at $n = 10^{11}$, 10^{12}, and 10^{13} cm^{-2} for different t_{ox} values.

screening phenomenon. At $n = 10^{12}$ cm^{-2} and $t_{\text{ox}} = 200$ nm, we have $\mu_{\text{IPP}} \approx 5500$ cm^{2}V^{-1}s^{-1}.

At $n = 10^{13}$ cm^{-2}, μ_{SPP} and μ_{IPP} do not change much with t_{ox}, because the electron-SPP and electron-IPP coupling coefficients are very similar over the relevant range of wave vectors ($0 < Q < 2K_F$) except at long wavelengths, as can be seen in Fig. 9. We also find that $\mu_{\text{IPP}} \gg \mu_{\text{SPP}}$ because there is little Landau damping and the effects of screening are very strong.

V. OTHER FACTORS AFFECTING ELECTRON MOBILITY

A. Electron density

We also calculate the conductance (σ_{IPP} and σ_{SPP}) and electron mobility (μ_{IPP} and μ_{SPP}) from $n = 10^{11}$ to 10^{13} cm^{-2} at $t_{\text{ox}} = 5$ and 30 nm, and plot the results in Fig. 11. The t_{ox} of 30 nm is chosen so that we can compare our results to the experimental data from a top-gated SLG structure in Ref. 24. The t_{ox} of 5 nm allows us to model the effects of a realistic ultrathin HfO$_2$ top gate. In Fig. 11(b), the μ_{IPP} for $t_{\text{ox}} = 30$ nm (solid line) and $t_{\text{ox}} = 5$ nm (dash-dot line) converge except at low densities ($n < 3 \times 10^{11}$ cm^{-2}), which we can see in the inset. This suggests that the μ_{IPP} does not vary significantly with the top oxide thickness. As $n \to 0$, μ_{IPP} and μ_{SPP} naturally converge as expected for either t_{ox} because the effects of plasmonic coupling and dynamic screening diminish.

At very low n, we have $\lim_{n\to 0} \mu_{\text{IPP}} = \mu_{\text{SPP}} \approx 1500$ cm^{2}V^{-1}s^{-1} for $t_{\text{ox}} = 30$ nm. Likewise, as the electron density increases and dynamic screening becomes stronger, μ_{IPP} increases and diverges from μ_{SPP}. A similar electron-density dependence on remote-phonon-limited channel mobility in Si was reported by Laikhtman and Solomon[33] and by Ren and co-workers.[34] In contrast, in simpler remote phonon scattering models,[9,12] the remote phonon-limited mobility μ_{RP} in graphene scales approximately as $n^{-\alpha}$, where $\alpha \approx 0.3$ to 0.5, i.e., the μ_{RP} *decreases* with electron density. We can fit the room temperature (300 K) electron density dependence of μ_{IPP} for $t_{\text{ox}} = 30$ nm with a simple empirical formula:

$$\mu_{\text{IPP}}(n) = \mu_{\text{SPP}}^{0} + \frac{\left(\mu_{\text{IPP}}^{\infty} - \mu_{\text{SPP}}^{0}\right) n}{\sqrt{n^2 + n_0^2}}, \tag{53}$$

where $\mu_{\text{SPP}}^{0} = 1500$ cm^{2}V^{-1}s^{-1} is the low electron density limit of μ_{SPP}, and $\mu_{\text{IPP}}^{\infty} = 28\,000$ cm^{2}V^{-1}s^{-1} is the maximum μ_{IPP} value; n_0 is a fitting parameter which we set equal to 6×10^{12} cm^{-2}. The formula in Eq. (53) yields a maximum μ_{IPP} value of 28 000 cm^{2}V^{-1}s^{-1}, which sets the upper bound to the electron mobility. At the technologically relevant density of $n = 10^{12}$ cm^{-2}, we find $\mu_{\text{IPP}} = 5500$ cm^{2}V^{-1}s^{-1} and $\mu_{\text{SPP}} = 1600$ cm^{2}V^{-1}s^{-1}.

We compare our mobility calculations to the experimental results in Ref. 24, where Zou *et al.* reported the data from transport measurements of very high quality HfO$_2$-covered, SiO$_2$-supported SLG. Using Matthiessen's rule, they estimate that remote phonons from the HfO$_2$ top gate set a maximum *field-effect* mobility of $\mu_{\text{FE}} \sim 20\,000$ cm^{2}V^{-1}s^{-1} at room temperature, based on their resistivity data over the electron density range of $n = 10^{12}$ to 3×10^{12} cm^{-2}. When the remote phonon contribution from the SiO$_2$ substrate is included, they obtain $\mu_{\text{FE}} \sim 17\,000$ cm^{2}V^{-1}s^{-1}. Remarkably, this falls within our range of calculated μ_{IPP} values between $n = 10^{12}$ and 10^{13} cm^{-2}: $\mu_{\text{IPP}} = 5500$ to 24 200 cm^{2}V^{-1}s^{-1}. Since $\mu_{\text{FE}} \gg \mu_{\text{SPP}} \approx 1500$ cm^{2}V^{-1}s^{-1}, it implies that plasmonic coupling and dynamic screening must be included in a realistic theory of remote phonon scattering.

Our mobility results between $n = 10^{12}$ and 3×10^{12} cm^{-2} are significantly lower ($\mu_{\text{IPP}} = 5500$ to 13 800 cm^{2}V^{-1}s^{-1} at 300 K) than their estimate because the dominant TO phonon frequency ω_{TO1} of HfO$_2$ in our model is 12.40 meV, whereas the Fourier transform infrared (FTIR) spectroscopy measurement of amorphous HfO$_2$ in Ref. 24 suggests a TO phonon frequency of around 40 meV. Using this value ($\omega_{\text{TO1}} = 40$ meV), we obtain instead $\mu_{\text{IPP}} = 7100$ to 15 100 cm^{2}V^{-1}s^{-1}, which is closer to the experimental estimate, for $n = 10^{12}$ to 3×10^{12} cm^{-2}. From this, we estimate that the oxides in HfO$_2$-covered, SiO$_2$-supported SLG set an electron mobility upper bound of 7100 cm^{2}V^{-1}s^{-1} at $n = 10^{12}$ cm^{-2}. We also fit the calculated data (with $\omega_{\text{TO1}} = 40$ meV) to Eq. (53), and find that it yields a maximum IPP-limited electron mobility of $\mu_{\text{IPP}}^{\infty} = 31\,000$ cm^{2}V^{-1}s^{-1}.

The temperature dependence of the different scattering processes can be used to determine their role in limiting electron mobility. Using a deformation potential approximation, Hwang and Das Sarma[35] estimate that the acoustic phonon-limited mobility[31] in SLG scales as $T^{-\alpha}$, where $\alpha = 1$ in the high temperature limit. This is supported by the DFT-based study by Kaasbjerg, Thygesen, and Jacobsen.[36] The temperature dependence of optical phonon-limited mobility is less clear. Fratini and Guinea suggest that it scales approximately as $\mu \propto e^{\hbar\omega_{\text{op}}/(k_B T)}$, where ω_{op} is the characteristic frequency of the optical phonon (intrinsic or remote). In the HfO$_2$-covered, SiO$_2$-supported SLG, there are four remote excitation or SPP frequencies in the surrounding oxides. Furthermore, the coupling with the graphene plasmons alters the dispersion of the SPP modes to give us wavelength-dependent excitation frequencies, as seen in Fig. 2. Hence it would be interesting to determine the temperature dependence of μ_{IPP}.

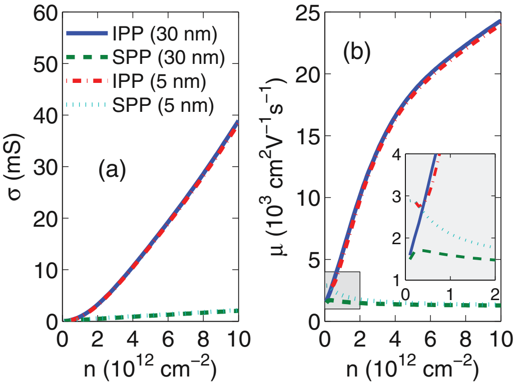

FIG. 11. (Color online) Plot of the (a) conductance and (b) mobility for the SPP and IPP remote phonon models. For $t_{\text{ox}} = 30$ nm, σ_{IPP} and μ_{IPP} (σ_{SPP} and μ_{SPP}) are drawn in solid (dashed) lines. For $t_{\text{ox}} = 5$ nm, σ_{IPP} and μ_{IPP} (σ_{SPP} and μ_{SPP}) are drawn in dash-dot (dotted) lines. The inset in (b) shows a zoomed-in plot of the mobility (μ_{SPP} and μ_{IPP}) for $t_{\text{ox}} = 5$ and 30 nm between $n = 0$ to 2×10^{12} cm^{-2}.

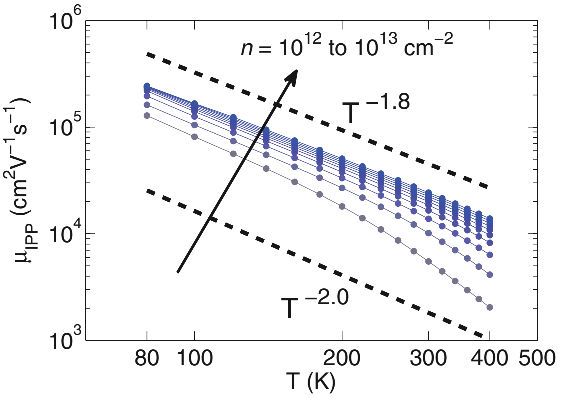

FIG. 12. (Color online) Plot of μ_{IPP} from $T = 80$ to 400 K for $n = 10^{12}$ to 10^{13} cm^{-2} at intervals of $\Delta T = 20$ K and $\Delta n = 10^{12}$ cm^{-2}. μ_{IPP} scales approximately as $\mu_{\mathrm{IPP}} \propto T^{-1.8}$ at $n = 10^{13}$ cm^{-2}.

We calculate μ_{IPP} from $T = 80$ to 400 K for $n = 10^{12}$ to 10^{13} cm^{-2} at intervals of $\Delta T = 20$ K and $\Delta n = 10^{12}$ cm^{-2}. The results are shown in Fig. 12. The first thing we notice is that μ_{IPP} scales as $T^{-\alpha}$, where α is between 1.8 and 2. At the high electron density of $n = 10^{13}$ cm^{-2}, we have a well-defined power law $\mu_{\mathrm{IPP}} \propto T^{-\alpha}$, where $\alpha \approx 1.8$. On the other hand, at the much lower electron density of $n = 10^{12}$ cm^{-2}, μ_{IPP} scales as T^{-2} for $T < 200$ K. As T increases beyond 200 K, interband transitions become more probable and μ_{IPP} deviates from this power law, as can be seen in Fig. 12. Our results suggest that at high temperatures and low electron densities, electron-IPP scattering may be the limiting factor in electron transport.

B. Interband transitions

When a electron in n-doped graphene is scattered by an IPP excitation of energy ω and wave vector $\mathbf{Q}$, it can undergo either an intraband transition ($s,\mathbf{K} \rightarrow s,\mathbf{K}+\mathbf{Q}$) within the conduction band ($s = 1$) or an interband transition ($s,\mathbf{K} \rightarrow s',\mathbf{K}+\mathbf{Q}, s \neq s'$) between the conduction ($s = 1$) and valence ($s = -1$) bands. In intraband transitions, the IPP excitation energy is $\omega < v_F Q$. In this case, the polarizability is ω independent, i.e., $\Pi(Q,\omega) = \Pi^{<}(Q)$. On the other hand, the IPP excitation energy in interband transitions is $\omega > v_F Q$, and the polarizability is ω dependent, i.e., $\Pi(Q,\omega) = \Pi^{>}(Q,\omega)$. Figure 2 shows that the IPP excitations that can produce intraband transitions are almost dispersionless. However, where $\omega > v_F Q$ and the IPP excitations are more Q dependent, i.e., more dispersive, the IPP excitations can be emitted or absorbed via interband transitions.

To understand the effect of the interband transitions, we compute μ_{IPP} with and without interband transitions between $n = 0$ and 10^{13} cm^{-2} at 300 K. The results are shown in Fig. 13(a) and suggest that the electron-IPP scattering is dominated by intraband processes. We find that there is a small but significant increase in μ_{IPP} when interband transitions are omitted. We plot in Fig. 13(b) $\Delta\mu_{\mathrm{IPP}}$, the increase in μ_{IPP}. $\Delta\mu_{\mathrm{IPP}}$ appears to be maximum at around $n = 10^{12}$ cm^{-2} and then decreases as n becomes larger, as expected because the higher chemical potential prohibits more interband transitions. Given that μ_{IPP} is only around a few thousand cm^{2}V^{-1}s^{-1} and comparable to $\Delta\mu_{\mathrm{IPP}}$ at low n, this suggests that the interband contribution to the electron mobility is much more important at low n and that the omission of interband processes can significantly overestimate the electron mobility.

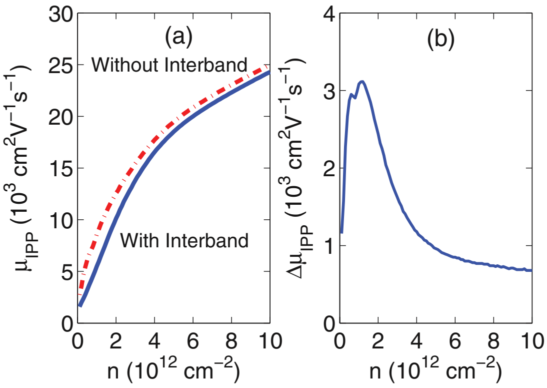

FIG. 13. (Color online) (a) Plot of the IPP-limited mobility (μ_{IPP}) with (solid) and without (dot-dash) interband transitions for $t_{\mathrm{ox}} = 30$ nm. Without interband transition, μ_{IPP} is higher. (b) Plot of the increase in μ_{IPP} ($\Delta\mu_{\mathrm{IPP}}$) with respect to the electron density n. The increase is maximum at around $n = 10^{12}$ cm^{-2}.

VI. SUMMARY AND CONCLUSION

We have developed a theory of remote phonon scattering in top-gated oxide that takes into account the thickness of the top dielectric and the plasmonic coupling to the surface polar phonon modes. We find that image charge screening by the top gate reduces the bare interaction between the SLG electrons and the SPPs as well as plasmonic coupling to SPP modes. The effect of the top gate screening on electron-IPP interaction is reduced at higher electron densities. We use our model to estimate the remote phonon-limited mobility μ_{RP} in HfO$_2$-covered, SiO$_2$-supported SLG. Our result agrees well with those estimated in experiments. Without dynamic screening, μ_{RP} is much lower than experimental estimates. At very low electron densities ($n = 10^{11}$ cm^{-2}), dynamic screening is unimportant and a thinner top oxide leads to a higher μ_{RP}. In contrast, at higher electron densities ($n = 10^{12}$ cm^{-2}), plasmonic coupling and dynamic screening become important, and a thinner top oxide reduces dynamic screening and leads to a lower μ_{RP}. However, at very high electron densities ($n \gg 10^{12}$ cm^{-2}), the top oxide thickness dependence of μ_{RP} vanishes. Based on the HfO$_2$ phonon parameters in Ref. 24, we estimate that the oxides in HfO$_2$-covered, SiO$_2$-supported SLG set an electron mobility upper bound of 7100 cm^{-2}V^{-1}s^{-1} at $n = 10^{12}$ cm^{-2} and an overall maximum IPP-limited electron mobility of $\mu_{\mathrm{IPP}}^{\infty} = 31\,000$ cm^{2}V^{-1}s^{-1}. Scattering by IPPs also leads to an approximate power law temperature dependence ($\mu_{\mathrm{IPP}} \propto T^{-\alpha}$, where $\alpha = 1.8$ to 2). We also show that electron-IPP scattering is dominated by intraband processes except at low electron densities.

ACKNOWLEDGMENTS

We acknowledge financial support from Texas Instruments, the Semiconductor Research Corporation, the Microelectronics Advanced Research Corporation, the Focus Center

Research Project for Materials, Structure and Devices (MSD) and Samsung Electronics Ltd. Valuable technical discussion was provided by Xia Hong (University of Nebraska-Lincoln), Emanuel Tutuc (University of Texas), Eric Pop (University of Illinois), Andrey Serov (University of Illinois), and David K. Ferry (Arizona State University).

---

[*] zhunyong.ong@utdallas.edu
[†] max.fischetti@utdallas.edu

[1] T. Palacios, A. Hsu, and H. Wang, IEEE Commun. Mag. **48**, 122 (2010).
[2] Y. Lin, C. Dimitrakopoulos, K. Jenkins, D. Farmer, H. Chiu, A. Grill, and P. Avouris, Science **327**, 662 (2010).
[3] M. Lemme, T. Echtermeyer, M. Baus, B. Szafranek, J. Bolten, M. Schmidt, T. Wahlbrink, and H. Kurz, Solid State Electron. **52**, 514 (2008).
[4] J. Moon, D. Curtis, S. Bui, M. Hu, D. Gaskill, J. Tedesco, P. Asbeck, G. Jernigan, B. VanMil, R. Myers-Ward *et al.* IEEE Electron Device Lett. **31**, 260 (2010).
[5] J. Pezoldt, C. Hummel, A. Hanisch, I. Hotovy, M. Kadlecikova, and F. Schwierz, Phys. Status Solidi C **7**, 390 (2010).
[6] J. Robinson, M. Wetherington, J. Tedesco, P. Campbell, X. Weng, J. Stitt, M. Fanton, E. Frantz, D. Snyder, B. VanMil *et al.* Nano Lett. **9**, 2873 (2009).
[7] X. Hong, K. Zou, A. M. DaSilva, C. H. Ahn, and J. Zhu, Solid State Commun. **152**, 1365 (2012).
[8] Z.-Y. Ong and M. V. Fischetti, Phys. Rev. B **86**, 121409 (2012).
[9] S. Fratini and F. Guinea, Phys. Rev. B **77**, 195415 (2008).
[10] S. Rotkin, V. Perebeinos, A. Petrov, and P. Avouris, Nano Lett. **9**, 1850 (2009).
[11] V. Perebeinos, S. Rotkin, A. Petrov, and P. Avouris, Nano Lett. **9**, 312 (2008).
[12] A. Konar, T. Fang, and D. Jena, Phys. Rev. B **82**, 115452 (2010).
[13] J. K. Viljas and T. T. Heikkilä, Phys. Rev. B **81**, 245404 (2010).
[14] Y. Liu, R. F. Willis, K. V. Emtsev, and T. Seyller, Phys. Rev. B **78**, 201403 (2008).
[15] Y. Liu and R. F. Willis, Phys. Rev. B **81**, 081406 (2010).
[16] Z. Fei, G. O. Andreev, W. Bao, L. M. Zhang, A. S. McLeod, C. Wang, M. K. Stewart, Z. Zhao, G. Dominguez, M. Thiemens, M. M. Fogler, M. J. Tauber, A. H. Castro-Neto, C. N. Lau, F. Keilmann, and D. N. Basov, Nano Lett. **11**, 4701 (2011).
[17] C. Jang, S. Adam, J. H. Chen, E. D. Williams, S. Das Sarma, and M. S. Fuhrer, Phys. Rev. Lett. **101**, 146805 (2008).
[18] N. Garces, V. Wheeler, J. Hite, G. Jernigan, J. Tedesco, N. Nepal, C. Eddy, and D. Gaskill, J. Appl. Phys. **109**, 124304 (2011).
[19] Z.-Y. Ong and M. V. Fischetti, Phys. Rev. B **86**, 165422 (2012).
[20] Z.-Y. Ong and M. V. Fischetti, Phys. Rev. B **86**, 199904(E) (2012).
[21] Z.-Y. Ong, M. V. Fischetti, A. Y. Serov, and E. Pop, Phys. Rev. B **87**, 195404 (2013).
[22] A. S. Price, S. M. Hornett, A. V. Shytov, E. Hendry, and D. W. Horsell, Phys. Rev. B **85**, 161411 (2012).
[23] B. Scharf, V. Perebeinos, J. Fabian, and P. Avouris, Phys. Rev. B **87**, 035414 (2013).
[24] K. Zou, X. Hong, D. Keefer, and J. Zhu, Phys. Rev. Lett. **105**, 126601 (2010).
[25] Z.-Y. Ong and M. V. Fischetti, Appl. Phys. Lett. **102**, 183506 (2013).
[26] M. V. Fischetti, D. A. Neumayer, and E. A. Cartier, J. Appl. Phys. **90**, 4587 (2001).
[27] S. Wang and G. Mahan, Phys. Rev. B **6**, 4517 (1972).
[28] B. Ridley, *Quantum Processes in Semiconductors* (Oxford University Press, New York, 1999).
[29] E. H. Hwang and S. Das Sarma, Phys. Rev. B **75**, 205418 (2007).
[30] B. Wunsch, T. Stauber, F. Sols, and F. Guinea, New J. Phys. **8**, 318 (2006).
[31] R. Shishir and D. Ferry, J. Phys. C **21**, 232204 (2009).
[32] G. Gilat and L. Raubenheimer, Phys. Rev. **144**, 390 (1966).
[33] B. Laikhtman and P. M. Solomon, J. Appl. Phys. **103**, 014501 (2008).
[34] Z. Ren, M. Fischetti, E. Gusev, E. Cartier, and M. Chudzik, *Electron Devices Meeting, 2003. IEDM'03 Technical Digest. IEEE International* (IEEE, New York, 2003), pp. 33–2.
[35] E. H. Hwang and S. Das Sarma, Phys. Rev. B **77**, 115449 (2008).
[36] K. Kaasbjerg, K. S. Thygesen, and K. W. Jacobsen, Phys. Rev. B **85**, 165440 (2012).